

Efficient formulation of a two-noded curved beam element under finite rotations

Martin Horák ·
Emma La Malfa Ribolla · Milan Jirásek

Received: date / Accepted: date

Abstract The paper extends the formulation of a 2D geometrically exact Navier-Bernoulli beam element proposed in our previous paper [9] to curved elastic beams. This formulation is based on equilibrium equations in their integrated form, combined with the kinematic relations and sectional equations. The resulting first-order differential equations are approximated by the finite difference scheme and the boundary value problem is converted to an initial value problem using the shooting method. Unlike standard finite element formulations, accuracy can be increased by refining the integration scheme on the element level while the number of global degrees of freedom are kept constant. The efficiency and accuracy are documented by five examples that cover circular, parabolic arches and a spiral-shaped beam. It is also shown that a cross effect in the relations between internal forces and deformation variables arises, i.e., the bending moment affects axial stretching and the normal force affects the curvature.

Keywords geometrically nonlinear beam · curved beam · large rotations · planar frame · shooting method

1 Introduction

Curved beam models are widely used in various engineering applications involving for example arches, pipes and bridge slab structures in civil engineering or lattice metamaterials, tires and rings in mechanical engineering. Often, these structures are discretized into multiple straight elements that represent the curved geometry

Martin Horák and Milan Jirásek
Thakurova 7, 166 29
Department of Mechanics, Czech Technical University in Prague, Czech Republic
E-mail: martin.horak@fsv.cvut.cz

Emma La Malfa Ribolla - Corresponding author
Viale delle Scienze, Ed. 8, 90128
Department of Engineering, University of Palermo, Italy
Tel.: +39-09123896570
E-mail: emma.lamalfaribolla@unipa.it

only approximately. The majority of contributions to the development of curved beam elements are based on the finite element (FE) method within the small-displacement theory and address shear and membrane locking caused by the coupling between bending and stretching [1, 6, 13, 24, 25, 27]. On the other hand, design and manufacturing of flexible as well as soft metamaterials have opened an area for the application of beams made of polymers or soft materials, for which large displacements and rotation may arise.

The key contributions to large-deformation analysis of thin beams are the theory of Reissner [16, 17], based on the extension of Timoshenko's assumption to finite deformations, and the FE formulation developed by Simo and his coworkers [20–23]. The geometrically exact beam theory is still attracting researchers, with recent developments in the isogeometric approach (e.g., [2, 12]) or in computational procedures related to the parameterisation of rotations using the rotation vector ([7, 10]). In a recent work [9] we have presented a numerical formulation for two-dimensional straight beams under large sectional rotations based on the shooting method: The boundary value problem is converted into an initial value problem handled by a finite difference scheme, and the estimated values used in artificially added initial conditions are iteratively adjusted until the boundary conditions on the opposite beam end are satisfied. On the global (structural) level, the governing equations are assembled in the same way as for a standard FE beam element with six degrees of freedom. It has been demonstrated that the advantage of this approach is a dramatic reduction of the number of global degrees of freedom, since the accuracy of the numerical approximation can be conveniently increased by refining the integration scheme on the element level instead of introducing additional global unknowns.

The present paper extends the geometrically exact formulation presented in [9] to curved beams undergoing large displacements and rotations. The theoretical framework is developed in Section 2 and the corresponding numerical procedures are described in Section 3. The efficiency and accuracy of the proposed method is illustrated in Section 4 by five examples, which treat circular and parabolic arches and a logarithmic spiral.

2 Beam with initial curvature

2.1 Kinematic description

The approach developed in [9] will now be extended to initially curved beams. Consider that the centerline of the undeformed beam is a planar curve of length L . An auxiliary curvilinear coordinate s is defined as the arc length measured along the undeformed centerline, with $s \in [0, L]$. For a given shape of the centerline, it is possible to specify function $\varphi_0(s)$ which describes the initial rotation of section s with respect to the left end section (this means that $\varphi_0(0) = 0$). Counterclockwise rotations are considered as positive. Displacement components u and w will be expressed with respect to a local Cartesian coordinate system xz that is attached to the left end section and follows its motion; see Fig. 1a.

The transformation of the beam from the undeformed state to the current one is decomposed into

- (A) a rigid-body translation and rotation that follows the motion of the left end section, and
- (B) a true deformation during which the left end section remains fixed.

Phase A can be handled by simple geometrical transformations and does not affect the end forces expressed with respect to the moving local coordinate system. It is therefore sufficient to focus on phase B and consider the left end of the beam as fixed. The black straight beam in Fig. 1a corresponds to a fictitious state used as a reference, while the initial stress-free configuration of the beam is plotted in red and the current deformed configuration in blue.

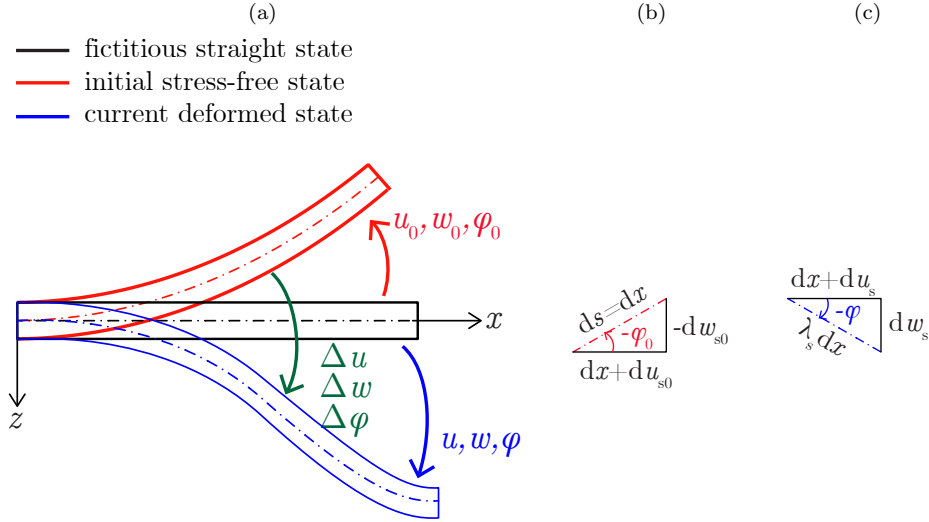


Fig. 1 (a) Coordinate system xz aligned with the left beam end, fictitious straight configuration (black), initial stress-free configuration (red), and current deformed configuration (blue); (b) infinitesimal triangle with hypotenuse on the centerline in the initial stress-free configuration; (c) infinitesimal triangle with hypotenuse on the centerline in the current deformed configuration

Fictitious displacements that describe the mapping of an arbitrary point (x, z) from its reference position in the fictitious straight state to its actual position in the initial stress-free configuration are denoted as u_0 and w_0 and considered as functions of x and z . Based on the standard assumption that all cross sections remain planar, these functions can be expressed as

$$u_0(x, z) = u_{s0}(x) + z \sin \varphi_0(x) \quad (1)$$

$$w_0(x, z) = w_{s0}(x) - z(1 - \cos \varphi_0(x)) \quad (2)$$

where u_{s0} and w_{s0} are functions of x that correspond to displacements of points on the centerline. Let us recall that φ_0 is the already introduced function defining the angle between a generic section and the left end section in the stress-free state. This angle at the same time corresponds to the rotation from the fictitious straight state to the initial stress-free state. It is also worth noting that the coordinate s

measured along the arc of the curved centerline in the stress-free state has the same value as the coordinate x measured along the Cartesian axis in the fictitious straight state, and in the subsequent derivations we will write all functions as dependent on x instead of s . In the same spirit, Cartesian coordinate z in the fictitious straight state corresponds to the coordinate that would be measured in the initial stress-free state in the direction normal to the curved centerline.

Functions u_{s0} , w_{s0} and φ_0 are supposed to be specified in advance but they are not independent. The length of the centerline must remain unaffected by the transformation from the fictitious straight reference configuration to the initial stress-free configuration, which is described by conditions

$$u'_{s0} = \cos \varphi_0 - 1 \quad (3)$$

$$w'_{s0} = -\sin \varphi_0 \quad (4)$$

in which the prime denotes the derivative with respect to x . Relations (3)–(4) follow from the geometry of the infinitesimal triangle depicted in Fig. 1b. By definition, cross sections in the initial state are perpendicular to the initial centerline, and so the angle by which the tangent to the centerline deviates from the x axis is the same as the angle φ_0 by which the section deviates from the z axis.

In principle it is possible to specify only function φ_0 and construct u_{s0} and w_{s0} by integrating equations (3)–(4) with initial conditions $u_{s0}(0) = 0$ and $w_{s0}(0) = 0$. Alternatively, one can characterize the initial shape by specifying functions u_{s0} and w_{s0} , making sure that they satisfy the constraint $(1 + u'_{s0})^2 + w'_{s0}{}^2 = 1$, and then evaluate function $\varphi_0 = -\arcsin w'_{s0}$. However, one should bear in mind that the description based on a given function φ_0 combined with relations (3)–(4) is fully general and permits arbitrary values of the “rotation” φ_0 , while the inverse relation $\varphi_0 = -\arcsin w'_{s0}$ is valid only as long as $\varphi_0 \in [-\pi/2, \pi/2]$. This is always true in the vicinity of the left end section but not necessarily along the whole beam. For instance, if we consider a circular arch of radius R , the initial shape is described by

$$\varphi_0(x) = \frac{x}{R} \quad (5)$$

$$u_{s0}(x) = R \sin \frac{x}{R} - x \quad (6)$$

$$w_{s0}(x) = R \left(\cos \frac{x}{R} - 1 \right) \quad (7)$$

from which

$$u'_{s0}(x) = \cos \frac{x}{R} - 1 \quad (8)$$

$$w'_{s0}(x) = -\sin \frac{x}{R} \quad (9)$$

Functions u_{s0} and w_{s0} defined in (6)–(7) satisfy the constraint $(1 + u'_{s0})^2 + w'_{s0}{}^2 = 1$, but the corresponding function φ_0 can be evaluated as $-\arcsin w'_{s0}$ only for $x \leq \pi R/2$. If the centerline length L exceeds $\pi R/2$, one needs to modify the formula for the inversion of (4) accordingly and set $\varphi_0 = \pi + \arcsin w'_{s0}$ for $x \in [\pi R/2, 3\pi R/2]$ etc.

The “total” centerline displacements, u_s and w_s , and the “total” rotation, φ , are understood as changes between the fictitious straight state and the final deformed configuration. They differ from the initial values by increments

$$\Delta u_s = u_s - u_{s0} \quad (10)$$

$$\Delta w_s = w_s - w_{s0} \quad (11)$$

$$\Delta \varphi = \varphi - \varphi_0 \quad (12)$$

that represent the actual displacements and rotation. Similar relations can be written for the displacements of an arbitrary point, u and w , for which the subscript “s” is dropped. In analogy to (1)–(2), the displacements of an arbitrary point can be expressed in terms of the centerline displacements and sectional rotation as

$$u(x, z) = u_s(x) + z \sin \varphi(x) \quad (13)$$

$$w(x, z) = w_s(x) - z(1 - \cos \varphi(x)) \quad (14)$$

2.2 Deformation variables

Let us proceed to the evaluation of strains. The sections are assumed to remain perpendicular to the centerline, and so the shear strains are neglected and it is sufficient to characterize the stretching in the direction parallel to the centerline. Consider a fiber segment parallel to the centerline and located at section x and at height z , which is in the reference straight configuration represented by an infinitesimal interval of length dx . In the deformed configuration, this segment is mapped on the hypotenuse of an orthogonal triangle with catheti $dx + du$ and dw and its length is

$$\overline{dx} = \sqrt{(dx + du)^2 + dw^2} = dx \sqrt{(1 + u')^2 + w'^2} \quad (15)$$

Making use of (1)–(2), we express the ratio between the current and reference fiber lengths as

$$\begin{aligned} \frac{\overline{dx}}{dx} &= \sqrt{(1 + u')^2 + w'^2} = \sqrt{(1 + u'_s + z\varphi' \cos \varphi)^2 + (w'_s - z\varphi' \sin \varphi)^2} = \\ &= \lambda_s + z\varphi' \end{aligned} \quad (16)$$

in which

$$\lambda_s = \sqrt{(1 + u'_s)^2 + w'^2_s} \quad (17)$$

is the centerline stretch.

When evaluating the actual physical stretch of a generic fiber, we need to take into account that the length of the considered fiber segment in the stress-free configuration is not dx but

$$dx_0 = (\lambda_{s0} + z\varphi'_0) dx = (1 + z\varphi'_0) dx \quad (18)$$

Here we have taken into account that

$$\lambda_{s0} = \sqrt{(1 + u'_{s0})^2 + w'^2_{s0}} = 1 \quad (19)$$

due to the constraint on the functions that define the initial shape (which follows from the assumption that coordinate x corresponds to the arc length measured along the centerline). Based on the above, the stretch of a generic fiber is given by

$$\lambda = \frac{\overline{dx}}{dx_0} = \frac{\lambda_s + z\varphi'}{1 + z\varphi'_0} = \frac{\lambda_s + z\kappa}{1 + z\kappa_0} \quad (20)$$

where $\kappa_0 = \varphi'_0$ is the initial curvature and $\kappa = \varphi'$ is the curvature in the deformed state. The fact that for $z = 0$ we obtain $\lambda = \lambda_s$ confirms that λ_s defined in (17) is the stretch evaluated at the centerline.

If we imagine the beam first as straight and then deform it to what we later consider as the initial configuration, the stretch would be given by $1 + z\kappa_0$. Measured with respect to the fictitious straight shape, the final stretch would be $\lambda_s + z\kappa$. However, since the fiber is actually stress-free in the initial (but curved) configuration, the effective stretch that it feels is the ratio $(\lambda_s + z\kappa)/(1 + z\kappa_0)$.

2.3 Internal forces

The next step is to set up the expression for the strain energy of the deformed beam and identify the internal forces as the variables work-conjugate with the sectional deformation variables λ_s and κ . Since the stress state at each material point is considered as uniaxial, it is sufficient to specify the strain energy density, \mathcal{E}_{int} , as function of the stretch, λ , and then integrate it over the volume. The density is understood here as strain energy per unit initial volume, i.e., volume in the stress-free but initially curved state of the beam. When integrating over the volume of the initially curved beam, we have to take into account that an infinitesimal segment of length dx measured along the centerline contains fibers whose length $(1 + z\kappa_0)dx$ varies as function of their distance from the centerline. The strain energy is therefore written as

$$E_{int} = \int_0^L \int_A (1 + z\kappa_0) \mathcal{E}_{int}(\lambda) dA dx \quad (21)$$

and its variation is

$$\delta E_{int} = \int_0^L \int_A (1 + z\kappa_0) \frac{\partial \mathcal{E}_{int}}{\partial \lambda} \delta \lambda dA dx \quad (22)$$

where A is the cross section and

$$\delta \lambda = \frac{\delta \lambda_s + z \delta \kappa}{1 + z\kappa_0} \quad (23)$$

is the variation of stretch. The derivative $\partial \mathcal{E}_{int} / \partial \lambda = \sigma$ is the stress work-conjugate with the Biot strain, because differentiation with respect to $\varepsilon = \lambda - 1$ gives the same result as differentiation with respect to λ . This stress can be interpreted as the normal component of the back-rotated first Piola-Kirchhoff stress (where the back rotation eliminates the effects of the cross-sectional rotation).

The expression for the strain energy variation can be further converted into

$$\begin{aligned}\delta E_{int} &= \int_0^L \int_A (1 + z\kappa_0) \sigma \frac{\delta\lambda_s + z\delta\kappa}{1 + z\kappa_0} dA dx = \int_0^L \int_A \sigma (\delta\lambda_s + z\delta\kappa) dA dx = \\ &= \int_0^L (N \delta\lambda_s + M \delta\kappa) dx\end{aligned}\quad (24)$$

in which

$$N = \int_A \sigma dA \quad (25)$$

$$M = \int_A z\sigma dA \quad (26)$$

are identified as the normal force and bending moment, playing the role of stress resultants that are work-conjugate with the centerline stretch and curvature.

If the expression for strain energy density is taken as quadratic, given by

$$\mathcal{E}_{int}(\lambda) = \frac{1}{2}E(\lambda - 1)^2 \quad (27)$$

where E is the Young modulus, the resulting stress-strain relation

$$\sigma = \frac{d\mathcal{E}_{int}(\lambda)}{d\lambda} = E(\lambda - 1) = E\varepsilon \quad (28)$$

is linear in terms of the Biot strain $\varepsilon = \lambda - 1$ and the (back-rotated) first Piola-Kirchhoff stress σ . However, since the distribution of stretches across the height of the section is not linear but is given by the rational function (20), the distribution of stresses across the section height is nonlinear even for a linear stress-strain law, and it is given by

$$\sigma = E \left(\frac{\lambda_s + z\kappa}{1 + z\kappa_0} - 1 \right) = E \frac{\lambda_s - 1 + z(\kappa - \kappa_0)}{1 + z\kappa_0} = E \frac{\varepsilon_s + z\Delta\kappa}{1 + z\kappa_0} \quad (29)$$

where

$$\varepsilon_s = \lambda_s - 1 \quad (30)$$

is the strain at the centerline and

$$\Delta\kappa = \kappa - \kappa_0 \quad (31)$$

is the difference between the curvatures in the deformed state and in the stress-free state.

Substituting the stress expressed from (29) into the integral formulae for internal forces, eqs. (25)–(26), we obtain

$$N = \int_A \sigma dA = E \int_A \frac{\varepsilon_s + z\Delta\kappa}{1 + z\kappa_0} dA = E \int_A \frac{dA}{1 + z\kappa_0} \varepsilon_s + E \int_A \frac{z dA}{1 + z\kappa_0} \Delta\kappa \quad (32)$$

$$M = \int_A z\sigma dA = E \int_A \frac{z\varepsilon_s + z^2\Delta\kappa}{1 + z\kappa_0} dA = E \int_A \frac{z dA}{1 + z\kappa_0} \varepsilon_s + E \int_A \frac{z^2 dA}{1 + z\kappa_0} \Delta\kappa \quad (33)$$

The resulting relations between internal forces and deformation variables can be written as

$$N = EA_{\kappa_0}\varepsilon_s + ES_{\kappa_0}\Delta\kappa \quad (34)$$

$$M = ES_{\kappa_0}\varepsilon_s + EI_{\kappa_0}\Delta\kappa \quad (35)$$

where

$$A_{\kappa_0} = \int_A \frac{dA}{1 + z\kappa_0} \quad (36)$$

$$S_{\kappa_0} = \int_A \frac{z dA}{1 + z\kappa_0} \quad (37)$$

$$I_{\kappa_0} = \int_A \frac{z^2 dA}{1 + z\kappa_0} \quad (38)$$

are modified sectional characteristics, dependent on the initial curvature κ_0 . They remain constant during the simulation and thus can be computed in advance, so their evaluation does not represent any problem even for general sections. For a rectangular section, they can be expressed analytically:

$$\begin{aligned} A_{\kappa_0} &= b_s \int_{-h_s/2}^{h_s/2} \frac{dA}{1 + z\kappa_0} = \frac{b_s}{\kappa_0} \ln \frac{2 + h_s\kappa_0}{2 - h_s\kappa_0} = \\ &= b_s h_s \left(1 + \frac{h_s^2 \kappa_0^2}{12} + \frac{h_s^4 \kappa_0^4}{80} + \frac{h_s^6 \kappa_0^6}{448} + \dots \right) \end{aligned} \quad (39)$$

$$\begin{aligned} S_{\kappa_0} &= b_s \int_{-h_s/2}^{h_s/2} \frac{z dA}{1 + z\kappa_0} = \frac{b_s}{\kappa_0^2} \left(h_s \kappa_0 - \ln \frac{2 + h_s\kappa_0}{2 - h_s\kappa_0} \right) = \\ &= -b_s h_s^2 \left(\frac{h_s \kappa_0}{12} + \frac{h_s^3 \kappa_0^3}{80} + \frac{h_s^5 \kappa_0^5}{448} + \dots \right) \end{aligned} \quad (40)$$

$$\begin{aligned} I_{\kappa_0} &= b_s \int_{-h_s/2}^{h_s/2} \frac{z^2 dA}{1 + z\kappa_0} = \\ &= \frac{b_s}{\kappa_0^3} \left(-h_s \kappa_0 + \ln \frac{2 + h_s\kappa_0}{2 - h_s\kappa_0} \right) = b_s h_s^3 \left(\frac{1}{12} + \frac{h_s^2 \kappa_0^2}{80} + \frac{h_s^4 \kappa_0^4}{448} + \dots \right) \end{aligned} \quad (41)$$

Note that $S_{\kappa_0} = -\kappa_0 I_{\kappa_0}$ and $A_{\kappa_0} = b_s h_s + \kappa_0^2 I_{\kappa_0}$, and so it is sufficient to evaluate I_{κ_0} . The dimensionless product $h_s \kappa_0$ is equal to the ratio h_s/R_0 where R_0 is the initial radius of curvature. If this ratio is 1:10, the relative difference between the generalized area A_{κ_0} and the standard area $A = b_s h_s$ is less than 10^{-3} , and for the moment of inertia it is 1.5×10^{-3} . The approximation

$$I_{\kappa_0} \approx b_s h_s^3 \left(\frac{1}{12} + \frac{h_s^2 \kappa_0^2}{80} \right) = \frac{b_s h_s^3}{12} \left(1 + 0.15 \frac{h_s^2}{R_0^2} \right) \quad (42)$$

is then sufficiently accurate.

2.4 Equilibrium equations

The equilibrium equations in their differential form could be derived from the stationarity conditions of the total potential energy functional using the standard variational approach. This procedure is described in detail in [9] and it will not be repeated here because the resulting equations

$$-(N \cos \varphi)' - \left(\frac{M'}{\lambda_s} \sin \varphi \right)' = 0 \quad (43)$$

$$(N \sin \varphi)' - \left(\frac{M'}{\lambda_s} \cos \varphi \right)' = 0 \quad (44)$$

are exactly the same as equations (26)–(27) in [9]. It is important to note that φ needs to be properly understood as the rotation of the section with respect to the fictitious straight configuration and not as the actual rotation with respect to the initial curved state, which would be $\Delta\varphi = \varphi - \varphi_0$. Furthermore, equations (43)–(44) can be integrated in closed form using the same approach as in [9], which finally leads to

$$N(x) = -X_{ab} \cos \varphi(x) + Z_{ab} \sin \varphi(x) \quad (45)$$

$$M(x) = -M_{ab} + X_{ab} w_s(x) - Z_{ab}(x + u_s(x)) \quad (46)$$

where X_{ab} , Z_{ab} and M_{ab} are integration constants that physically correspond to the end forces and end moment acting on the left end of the beam. Again, φ , u_s and w_s are the rotation and displacements with respect to the fictitious straight configuration, and the components of end forces are expressed with respect to the local xz coordinate system attached to the left end. Of course, equations (45)–(46) could be set up directly as equilibrium conditions deduced from a free-body diagram, but it is reassuring that they can be derived variationally and that the internal forces (primarily defined as work conjugates of the deformation variables) have indeed their usual meaning.

2.5 Treatment of the governing equations

The approach used here when setting up the relations between the generalized end forces (i.e., end forces and moments) and the generalized end displacements (i.e., end displacements and rotations) follows the main idea described in [9]. Instead of approximating the centerline displacement functions by a linear combination of pre-selected functions (e.g., polynomials) and enforcing equilibrium in the weak sense, we consider the integrated equilibrium equations (45)–(46) and combine them with the sectional constitutive equations (34)–(35) and with a set of three first-order differential equations

$$\varphi' = \kappa \quad (47)$$

$$u_s' = \lambda_s \cos \varphi - 1 \quad (48)$$

$$w_s' = -\lambda_s \sin \varphi \quad (49)$$

which link the centerline displacement functions u_s and w_s and the sectional rotation function φ to the deformation variables—centerline stretch λ_s and curvature

κ . Equation (47) directly follows from the definition of the curvature, specified in the text after equation (20), while equations (48)–(49) follow from the geometry of an orthogonal triangle with hypotenuse given by a deformed centerline segment of length $\lambda_s dx$ inclined by φ with respect to the horizontal axis; see Fig. 1c.

One component of the outlined approach is the evaluation of the deformation variables from the internal forces, which is based on the inverted form of equations (34)–(35). For a general section, the inverted equations read

$$\varepsilon_s = \frac{I_{\kappa_0} N - S_{\kappa_0} M}{E(A_{\kappa_0} I_{\kappa_0} - S_{\kappa_0}^2)} \quad (50)$$

$$\Delta\kappa = \frac{-S_{\kappa_0} N + A_{\kappa_0} M}{E(A_{\kappa_0} I_{\kappa_0} - S_{\kappa_0}^2)} \quad (51)$$

In the special case of a rectangular section, one can further exploit the fact that $S_{\kappa_0} = -\kappa_0 I_{\kappa_0}$ and $A_{\kappa_0} = A + \kappa_0^2 I_{\kappa_0}$, which leads to simplified equations

$$\varepsilon_s = \frac{N + \kappa_0 M}{EA} \quad (52)$$

$$\Delta\kappa = \frac{\kappa_0 N}{EA} + \frac{M}{EI_{\kappa_0}} + \frac{\kappa_0^2 M}{EA} = \frac{M}{EI_{\kappa_0}} + \kappa_0 \varepsilon_s \quad (53)$$

One could now express the internal forces on the right-hand sides of (52)–(53) using the integrated equilibrium equations (45)–(46), and then transform the deformation variables ε_s and $\Delta\kappa$ into $\lambda_s = 1 + \varepsilon_s$ and $\kappa = \kappa_0 + \Delta\kappa$ and substitute the resulting expressions into the right-hand sides of (47)–(49). This would lead to a set of three ordinary differential equations for functions u_s , w_s and φ_s , with all the other unknown functions eliminated. However, for the purpose of numerical treatment, it is preferred to keep the equations separate and process them one by one, because the procedure will be more transparent and individual operations will have a clear physical meaning.

3 Numerical procedures

3.1 Choice of primary unknown functions

Based on the theoretical description developed in the preceding section, a natural choice of the primary unknown functions would be the centerline displacements u_s and w_s and the sectional rotation φ . However, we should bear in mind that these kinematic variables describe changes of the current beam state with respect to the fictitious straight state. A potential disadvantage of the approach based on such “total” displacements is that even the initial stress-free shape would be computed numerically with some error, even though functions u_{s0} , w_{s0} and φ_0 that characterize the stress-free state are assumed to be known. One also needs to take into account that since the computed “total” displacements and rotation at the right end of the beam, $u_s(L)$, $w_s(L)$ and $\varphi(L)$, are referred to the fictitious straight shape, they do not correspond to the actual displacements and rotation of the joint to which the right end is attached. The joint displacements and rotation are in fact $\Delta u_s(L)$, $\Delta w_s(L)$ and $\Delta\varphi(L)$. For instance, if the beam ends do not move at all, the target values that should be obtained by the shooting method

(to be described in Section 3.2) would not be zero but $u_{s0}(L)$, $w_{s0}(L)$ and $\varphi_0(L)$. These corrections would need to be included in the expressions for the residual used by the shooting method.

The above considerations motivate an alternative choice of displacements and rotation with respect to the stress-free configuration, Δu_s , Δw_s and $\Delta\varphi$, as the primary unknown functions. In terms of these “true” displacements and rotation, equations (47)–(49) can be rewritten as

$$\Delta\varphi' = \Delta\kappa \quad (54)$$

$$\Delta u'_s = (1 + \varepsilon_s) \cos(\varphi_0 + \Delta\varphi) - \cos \varphi_0 \quad (55)$$

$$\Delta w'_s = -(1 + \varepsilon_s) \sin(\varphi_0 + \Delta\varphi) + \sin \varphi_0 \quad (56)$$

These equations have been obtained by combining (47)–(49) with (10)–(12), (3)–(4) and (30)–(31). Function φ_0 is known (it specifies the initial geometry) and the deformation variables ε_s and $\Delta\kappa$ are directly evaluated from N and M using (52)–(53). Of course, when the internal forces are computed based on equations (45)–(46), the displacements and rotation must be substituted in their total form, i.e., Δu_s , Δw_s and $\Delta\varphi$ must be increased by the known values of u_{s0} , w_{s0} and φ_0 .

3.2 Shooting method

From the mathematical point of view, the problem that we need to solve looks like an initial value problem, because equations (54)–(56) are first-order differential equations for $\Delta\varphi$, Δu_s and Δw_s and the initial values $\Delta\varphi(0) = 0$, $\Delta u_s(0) = 0$ and $\Delta w_s(0) = 0$ are known (due to the definition of the local coordinate system that remains firmly attached to the left end section). However, in order to proceed with the integration, one also needs to know the left-end forces X_{ab} and Z_{ab} and the left-end moment M_{ab} , which are used when expressing the internal forces according to (45)–(46).

In the context of structural analysis, the beam under consideration is attached to joints that link it to other beams, and the joint displacements and rotations play the role of basic global unknowns. Therefore, a typical task at the beam element level is to evaluate the end forces and moments (at both ends) generated by prescribed displacements and rotations of the joints. Numerical treatment of this task can be based on a special version of the shooting method, i.e., of the method that converts a boundary value problem into an initial value problem with an iterative modification of those initial values that are not known. These values are first guessed and then repeatedly corrected until the boundary conditions on the opposite end of the interval are satisfied with sufficient accuracy. In the present setting, the left-end forces X_{ab} and Z_{ab} and the left-end moment M_{ab} need to be adjusted until the numerically computed displacements and rotation of the right end (with respect to the coordinate system attached to the left end) become equal to the target values determined from the prescribed joint displacements and rotations. This iterative process at the beam element level is embedded in the global iteration of joint displacements and rotations leading to satisfaction of joint equilibrium conditions.

To formalize the computational procedure outlined above, let us introduce the column matrix of the left end generalized forces,

$$\mathbf{f}_{ab} = \begin{pmatrix} X_{ab} \\ Z_{ab} \\ M_{ab} \end{pmatrix} \quad (57)$$

and the column matrix of the right end generalized displacements,

$$\mathbf{u}_b = \begin{pmatrix} u_b \\ w_b \\ \varphi_b \end{pmatrix} \quad (58)$$

Numerical integration along the beam, starting from zero values of generalized displacements at the left end and using generalized forces \mathbf{f}_{ab} , leads to the values of generalized displacements at the right end. This is formally described by the mapping

$$\mathbf{g}(\mathbf{f}_{ab}) = \begin{pmatrix} \Delta u_s(L; X_{ab}, Z_{ab}, M_{ab}) \\ \Delta w_s(L; X_{ab}, Z_{ab}, M_{ab}) \\ \Delta \varphi(L; X_{ab}, Z_{ab}, M_{ab}) \end{pmatrix} \quad (59)$$

where for instance $\Delta u_s(L; X_{ab}, Z_{ab}, M_{ab})$ means the value of function Δu_s at $x = L$ determined with the left end forces set to X_{ab} and Z_{ab} and the left end moment to M_{ab} .

For given values of \mathbf{u}_b , condition

$$\mathbf{g}(\mathbf{f}_{ab}) = \mathbf{u}_b \quad (60)$$

represents a set of three nonlinear equations for unknowns \mathbf{f}_{ab} . The solution is found by the Newton-Raphson method, using the recursive formula

$$\mathbf{f}_{ab}^{(k+1)} = \mathbf{f}_{ab}^{(k)} + \mathbf{G}^{-1} \left(\mathbf{f}_{ab}^{(k)} \right) \left(\mathbf{u}_b - \mathbf{g} \left(\mathbf{f}_{ab}^{(k)} \right) \right), \quad k = 0, 1, 2, \dots \quad (61)$$

where

$$\mathbf{G} = \frac{\partial \mathbf{g}}{\partial \mathbf{f}_{ab}} \quad (62)$$

is the Jacobi matrix of mapping \mathbf{g} .

Note that the target values of $\Delta u_s(L)$, $\Delta w_s(L)$ and $\Delta \varphi(L)$ are the true displacements and rotation of the joint attached to the right end of the beam. Of course, the displacement components must be taken with respect to the local beam coordinate system aligned with the left end. The advantage of the approach based on displacements and rotation with respect to the initial shape is that, for this choice, $\mathbf{g}(\mathbf{0}) = \mathbf{0}$ holds exactly, even when the mapping \mathbf{g} is evaluated numerically, and so for zero prescribed displacements of the joints, leading to $\mathbf{u}_b = \mathbf{0}$, equation (60) yields zero end forces, $\mathbf{f}_{ab} = \mathbf{0}$. This would not be the case if the numerical integration used the “total displacements” as primary unknowns, because the initial shape would not be captured exactly by the numerical approximation.

3.3 Algorithms

Numerical algorithms for evaluation of function \mathbf{g} will be developed in Sections 3.3.1–3.3.2 and the algorithm for evaluation of the Jacobi matrix \mathbf{G} will be described in Section 3.3.3. Approximation of the governing equations is based on finite difference expressions. The interval $[0, L]$ is divided into N segments of equal length $h = L/N$, which connect the grid points $x_i = ih$, $i = 0, 1, 2, \dots, N$. The approximate values of various quantities at point x_i will be denoted by subscript i . To increase the accuracy, in some cases it is beneficial to deal with approximate values at the midpoint of segment number i , which will be denoted by subscripts $i - 1/2$.

3.3.1 Circular arch with rectangular section

To clearly show the structure of the algorithm, let us first consider the special case of a circular arch of radius R with a rectangular cross section of width b_s and depth h_s . In this case, the initial curvature $\kappa_0 = 1/R$ (convex shape) or $\kappa_0 = -1/R$ (concave shape) is constant and sectional parameters are constant as well, so they do not need to be recomputed in each step.

1. Evaluate sectional characteristics $A = b_s h_s$, $I = b_s h_s^3/12$, $I_{\kappa_0} = (1 + 0.15 h_s^2/R^2) I$.
2. Set initial values

$$\Delta u_0 = 0 \quad (63)$$

$$\Delta w_0 = 0 \quad (64)$$

$$\Delta \varphi_0 = 0 \quad (65)$$

$$M_0 = -M_{ab} \quad (66)$$

$$\varepsilon_0 = (-X_{ab} + M_0/R)/EA \quad (67)$$

$$\Delta \kappa_0 = \varepsilon_0/R + M_0/EI_{\kappa_0} \quad (68)$$

3. For $i = 1, 2, \dots, N$ evaluate

$$\Delta \varphi_{i-1/2} = \Delta \varphi_{i-1} + \Delta \kappa_{i-1} \Delta x/2 \quad (69)$$

$$\varphi_{i-1/2} = \Delta \varphi_{i-1/2} + x_{i-1/2}/R \quad (70)$$

$$N_{i-1/2} = -X_{ab} \cos \varphi_{i-1/2} + Z_{ab} \sin \varphi_{i-1/2} \quad (71)$$

$$\varepsilon_{i-1/2} = (N_{i-1/2} + M_{i-1}/R)/EA \quad (72)$$

$$\Delta u_i = \Delta u_{i-1} + [(1 + \varepsilon_{i-1/2}) \cos \varphi_{i-1/2} - \cos(x_{i-1/2}/R)] \Delta x \quad (73)$$

$$\Delta w_i = \Delta w_{i-1} + [\sin(x_{i-1/2}/R) - (1 + \varepsilon_{i-1/2}) \sin \varphi_{i-1/2}] \Delta x \quad (74)$$

$$\tilde{x}_i = R \sin(x_i/R) + \Delta u_i \quad (75)$$

$$w_i = R(\cos(x_i/R) - 1) + \Delta w_i \quad (76)$$

$$M_i = -M_{ab} + X_{ab} w_i - Z_{ab} \tilde{x}_i \quad (77)$$

$$\varepsilon_i = (N_{i-1/2} + M_i/R)/EA \quad (78)$$

$$\Delta \kappa_i = \varepsilon_i/R + M_i/EI_{\kappa_0} \quad (79)$$

$$\Delta \varphi_i = \Delta \varphi_{i-1/2} + \Delta \kappa_i \Delta x/2 \quad (80)$$

4. The resulting values of right-end displacements and rotation are $u_b = \Delta u_N$, $w_b = \Delta w_N$ and $\varphi_b = \Delta \varphi_N$.

This algorithm has a similar structure to the one developed in [9] for a straight beam. It is fully explicit and at the same time second-order accurate because time derivatives are replaced either by central differences, or by a sequence of two half-steps that use a forward difference combined with a backward difference. For instance, equation (54) is integrated in two half-steps described by (69) and (80), the first one being based on a forward difference and the second on a backward difference. For an initially straight beam, the axial strain depends only on the normal force, which can be determined from the sectional rotation without knowing the displacements, and the curvature depends only on the bending moment, which can be determined from the displacements without knowing the rotation. In that case, integration of equation (54) in two half-steps described by (69) and (80) corresponds to the trapezoidal rule, and integration of equations (55)–(56) described by (73)–(74) corresponds to the midpoint rule. The initial curvature introduces a slight coupling but the effects of the normal force on the change of curvature and of the bending moment on the axial strain remains small. This is why the accuracy is not substantially compromised if

- the evaluation of the axial strain at midstep described by (72) is based on the normal force at midstep and the bending moment at the beginning of the step, and
- the evaluation of the curvature change at the end of the step described by (79) is based on the bending moment at the end of the step combined with the normal force at midstep; see (78).

Using this scheme, it is sufficient to evaluate the normal force only at midstep and the bending moment only at the end of the step. One can avoid the evaluation of the bending moment and displacements at midstep and of the normal force at the end of the step, which would involve additional calculations without a substantial increase in accuracy. Note that \tilde{x}_i , w_i and ε_i computed in (75)–(76) and (78) are auxiliary variables, which are directly used in (77) and (79) but do not need to be stored.

3.3.2 General case

For a beam with arbitrary initial geometry, the initial shape is supposed to be described by given functions u_{s0} , w_{s0} and φ_0 , from which it is possible to derive the initial curvature function, $\kappa_0 = \varphi'_0$. Based on the shape and dimensions of the cross section, one can determine the generalized sectional characteristics A_{κ_0} , S_{κ_0} and I_{κ_0} . We assume here that the section does not vary along the centerline, and so the characteristics are treated as given constants. The algorithm can be generalized as follows:

1. Evaluate sectional characteristics A_{κ_0} , S_{κ_0} and I_{κ_0} given by (36)–(38) and $D_{\kappa_0} = E(A_{\kappa_0} I_{\kappa_0} - S_{\kappa_0}^2)$.

2. Set initial values

$$\Delta u_0 = 0 \quad (81)$$

$$\Delta w_0 = 0 \quad (82)$$

$$\Delta \varphi_0 = 0 \quad (83)$$

$$M_0 = -M_{ab} \quad (84)$$

$$\kappa_{0,0} = \kappa_0(0) \quad (85)$$

$$\varepsilon_0 = \frac{-I_{\kappa_0} X_{ab} - S_{\kappa_0} M_0}{D_{\kappa_0}} \quad (86)$$

$$\Delta \kappa_0 = \frac{S_{\kappa_0} X_{ab} + A_{\kappa_0} M_0}{D_{\kappa_0}} \quad (87)$$

3. For $i = 1, 2, \dots, N$ evaluate

$$\Delta \varphi_{i-1/2} = \Delta \varphi_{i-1} + \Delta \kappa_{i-1} \Delta x / 2 \quad (88)$$

$$\varphi_{i-1/2} = \varphi_0(x_{i-1/2}) + \Delta \varphi_{i-1/2} \quad (89)$$

$$N_{i-1/2} = -X_{ab} \cos \varphi_{i-1/2} + Z_{ab} \sin \varphi_{i-1/2} \quad (90)$$

$$\varepsilon_{i-1/2} = \frac{I_{\kappa_0} N_{i-1/2} - S_{\kappa_0} M_{i-1}}{D_{\kappa_0}} \quad (91)$$

$$\Delta u_i = \Delta u_{i-1} + [(1 + \varepsilon_{i-1/2}) \cos \varphi_{i-1/2} - \cos \varphi_0(x_{i-1/2})] \Delta x \quad (92)$$

$$\Delta w_i = \Delta w_{i-1} + [\sin \varphi_0(x_{i-1/2}) - (1 + \varepsilon_{i-1/2}) \sin \varphi_{i-1/2}] \Delta x \quad (93)$$

$$M_i = -M_{ab} + X_{ab}(w_0(x_i) + \Delta w_i) - Z_{ab}(x_i + u_0(x_i) + \Delta u_i) \quad (94)$$

$$\Delta \kappa_i = \frac{-S_{\kappa_0} N_{i-1/2} + A_{\kappa_0} M_i}{D_{\kappa_0}} \quad (95)$$

$$\Delta \varphi_i = \Delta \varphi_{i-1/2} + \Delta \kappa_i \Delta x / 2 \quad (96)$$

4. The resulting values of right-end displacements and rotation are $u_b = \Delta u_N$, $w_b = \Delta w_N$ and $\varphi_b = \Delta \varphi_N$.

3.3.3 Jacobi matrix

The foregoing algorithms define the mapping \mathbf{g} of the generalized left-end forces \mathbf{f}_{ab} on the generalized right-end displacements $\mathbf{g}(\mathbf{f}_{ab})$, which is needed for the evaluation of the left-hand side of (60). For iterative solution of equations (60) by the Newton-Raphson method, one also needs the Jacobi matrix of mapping \mathbf{g} , i.e., the matrix

$$\mathbf{G} = \frac{\partial \mathbf{g}}{\partial \mathbf{f}_{ab}} \quad (97)$$

which contains derivatives of the right-end displacements and rotation with respect to the left-end forces and moment.

The entries of the Jacobi matrix are evaluated numerically using the linearized version of the computational scheme. Suppose that the input values of left-end forces X_{ab} , Z_{ab} and M_{ab} are perturbed by infinitesimal increments dX_{ab} , dZ_{ab}

and dM_{ab} . The corresponding infinitesimal changes of displacements and rotations along the beam can be computed from the linearized form of equations (88)–(96), which reads

$$d\varphi_{i-1/2} = d\varphi_{i-1} + d\kappa_{i-1}\Delta x/2 \quad (98)$$

$$dN_{i-1/2} = -dX_{ab} \cos \varphi_{i-1/2} + dZ_{ab} \sin \varphi_{i-1/2} + X_{ab} \sin \varphi_{i-1/2} d\varphi_{i-1/2} + Z_{ab} \cos \varphi_{i-1/2} d\varphi_{i-1/2} \quad (99)$$

$$d\varepsilon_{i-1/2} = \frac{I_{\kappa_0} dN_{i-1/2} - S_{\kappa_0} dM_{i-1}}{D_{\kappa_0}} \quad (100)$$

$$du_i = du_{i-1} + [d\varepsilon_{i-1/2} \cos \varphi_{i-1/2} - (1 + \varepsilon_{i-1/2}) \sin \varphi_{i-1/2} d\varphi_{i-1/2}] \Delta x \quad (101)$$

$$dw_i = dw_{i-1} + [-d\varepsilon_{i-1/2} \sin \varphi_{i-1/2} - (1 + \varepsilon_{i-1/2}) \cos \varphi_{i-1/2} d\varphi_{i-1/2}] \Delta x \quad (102)$$

$$dM_i = -dM_{ab} + dX_{ab}(w_0(x_i) + \Delta w_i) - dZ_{ab}(x_i + u_0(x_i) + \Delta u_i) + X_{ab} dw_i - Z_{ab} du_i \quad (103)$$

$$d\kappa_i = \frac{-S_{\kappa_0} dN_{i-1/2} + A_{\kappa_0} dM_i}{D_{\kappa_0}} \quad (104)$$

$$d\varphi_i = d\varphi_{i-1/2} + d\kappa_i \Delta x/2 \quad (105)$$

The values of du_0 , dw_0 and $d\varphi_0$ are set to zero, because the zero values of Δu_0 , Δw_0 and $\Delta \varphi_0$ are fixed; see (81)–(83). The value of $d\kappa_0$ is obtained as $(S_{\kappa_0} dX_{ab} + A_{\kappa_0} dM_0)/D_{\kappa_0}$.

If we set $dX_{ab} = 1$ and $dZ_{ab} = dM_{ab} = 0$, the resulting values of du_N , dw_N and $d\varphi_N$ will correspond to the first column of the Jacobi matrix \mathbf{G} . They are evaluated using the adapted scheme with $d\kappa_0 = S_{\kappa_0}/D_{\kappa_0}$ and

$$d\varphi_{i-1/2} = d\varphi_{i-1} + d\kappa_{i-1}\Delta x/2 \quad (106)$$

$$dN_{i-1/2} = -\cos \varphi_{i-1/2} + \sin \varphi_{i-1/2} d\varphi_{i-1/2} + Z_{ab} \cos \varphi_{i-1/2} d\varphi_{i-1/2} \quad (107)$$

$$d\varepsilon_{i-1/2} = \frac{I_{\kappa_0} dN_{i-1/2} - S_{\kappa_0} dM_{i-1}}{D_{\kappa_0}} \quad (108)$$

$$du_i = du_{i-1} + [d\varepsilon_{i-1/2} \cos \varphi_{i-1/2} - (1 + \varepsilon_{i-1/2}) \sin \varphi_{i-1/2} d\varphi_{i-1/2}] \Delta x \quad (109)$$

$$dw_i = dw_{i-1} - [d\varepsilon_{i-1/2} \sin \varphi_{i-1/2} + (1 + \varepsilon_{i-1/2}) \cos \varphi_{i-1/2} d\varphi_{i-1/2}] \Delta x \quad (110)$$

$$dM_i = w_0(x_i) + \Delta w_i + X_{ab} dw_i - Z_{ab} du_i \quad (111)$$

$$\kappa_{0,i} = \kappa_0(x_i) \quad (112)$$

$$I_{\kappa_{0,i}} = (1 + 0.15h_s^2 \kappa_{0,i}^2) I \quad (113)$$

$$d\varepsilon_i = (dN_{i-1/2} + \kappa_{0,i} dM_i)/EA \quad (114)$$

$$d\kappa_i = \frac{-S_{\kappa_0} dN_{i-1/2} + A_{\kappa_0} dM_i}{D_{\kappa_0}} \quad (115)$$

$$d\varphi_i = d\varphi_{i-1/2} + d\kappa_i \Delta x/2 \quad (116)$$

The other two columns are obtained in an analogous fashion. In practice, the evaluation of (106)–(116) in a loop over $i = 1, 2, \dots, N$ is performed simultaneously with the evaluation of (88)–(96), so that various auxiliary values such as $\cos \varphi_{i-1/2}$, $\sin \varphi_{i-1/2}$ or $\varepsilon_{i-1/2}$ can be reused.

3.4 Transformation to global coordinates

Suppose that the algorithms described in Section 3.3 have been implemented and equations (60) can be solved numerically based on the iterative scheme (61). The prescribed values of right-end displacements \mathbf{u}_b on the right-hand side of (60) as well as the resulting left-end forces \mathbf{f}_{ab} are expressed in a local coordinate system xz , with the origin located at the left end of the beam in the deformed configuration and with the x axis in the direction of the tangent to the deformed centerline at the left end. Now we need to link the local components of forces and displacements to the components expressed with respect to the global coordinate system used for the whole structural model, which will be denoted by a superscript G .

The initial geometry is described by global coordinates of the joints connected by the beam, i.e., x_a^G and z_a^G at the left end and x_b^G and z_b^G at the right end, and also by the beam length measured along the centerline, L , and by functions u_{s0} , w_{s0} , φ_0 and κ_0 that specify the curved shape of the beam. These functions are not independent, and in principle it would be sufficient to specify the curvature, κ_0 , because the rotation, φ_0 , could be computed by integrating κ_0 and imposing initial condition $\varphi_0(0) = 0$, and the functions describing the centerline, u_{s0} and w_{s0} , could be computed by integrating equations (3)–(4) and imposing initial conditions $u_{s0}(0) = 0$ and $w_{s0}(0) = 0$. Instead of performing these operations numerically or developing complicated rules for symbolic integration, the implementation in OOFEM [14, 15] leaves it up to the user to prepare all needed functions and specify them on input, making sure that they are consistent.

For the purpose of transformation between local and global coordinate systems, we need to characterize the angle α_{ab} by which the local axes are rotated (clockwise) with respect to the global axes. Suppose that α_{0ab} is the value of this angle in the initial stress-free state, which can be determined from the given geometrical data. During the deformation process, the local coordinate system rotates with the left end joint, and so

$$\alpha_{ab} = \alpha_{0,ab} - \varphi_a^G \quad (117)$$

where φ_a^G is the rotation of the left joint (positive counterclockwise). Another quantity that will play a role in the transformations is the angle by which the beam chord deviates from the local x -axis. The value of this angle in the initial stress-free state, denoted as β_{0ab} , can easily be deduced from the description of the initial beam shape.

As already explained in Section 2.1, the total transformation of the beam can be conceptually decomposed into two parts: (A) rigid-body motion and (B) pure deformation. We can imagine that during stage A the beam moves as a rigid body such that it gets translated by u_a^G and w_a^G and then rotated about the left end by φ_a^G counterclockwise. This part of the overall motion does not affect the deformation state of the beam and has no effect on the end forces and moments, provided that their components are expressed with respect to a coordinate system that rotates with the beam.

During stage B, the left end remains fixed while the right end is moved to its actual position in the deformed configuration and the right end section is rotated by $\varphi_b^G - \varphi_a^G$. The displacements of the right end experienced during this second stage and expressed with respect to the local coordinate system attached to the

left end are

$$u_b = (u_b^G - u_a^G) \cos \alpha_{ab} + (w_b^G - w_a^G) \sin \alpha_{ab} + L_{ab}(\cos(\beta_{0ab} + \varphi_a^G) - \cos \beta_{0ab}) \quad (118)$$

$$w_b = -(u_b^G - u_a^G) \sin \alpha_{ab} + (w_b^G - w_a^G) \cos \alpha_{ab} + L_{ab}(\sin(\beta_{0ab} + \varphi_a^G) - \sin \beta_{0ab}) \quad (119)$$

where L_{ab} is the length of the initial chord, see (130), and the rotation is

$$\varphi_b = \varphi_b^G - \varphi_a^G \quad (120)$$

Therefore, if the global displacements and rotations are prescribed, they can be transformed into the local displacements and rotation of the right end with respect to the left end, which are assembled into the column matrix \mathbf{u}_b . The corresponding column matrix of left-end forces \mathbf{f}_{ab} , obtained by solving equations (59) and formally denoted as $\mathbf{g}^{-1}(\mathbf{u}_b)$, has components X_{ab} , Z_{ab} and M_{ab} . Here, M_{ab} is directly the end moment acting at the left end, while the end forces must be transformed into the global components

$$X_{ab}^G = X_{ab} \cos \alpha_{ab} - Z_{ab} \sin \alpha_{ab} \quad (121)$$

$$Z_{ab}^G = X_{ab} \sin \alpha_{ab} + Z_{ab} \cos \alpha_{ab} \quad (122)$$

Finally, equilibrium equations written for the whole beam lead to expressions for the right-end forces

$$X_{ba}^G = -X_{ab}^G \quad (123)$$

$$Z_{ba}^G = -Z_{ab}^G \quad (124)$$

and the right-end moment

$$M_{ba} = -M_{ab} + X_{ab}(w_{s0}(L) + w_b) - Z_{ab}(L + u_{s0}(L) + u_b) \quad (125)$$

The angle characterizing the initial deviation of the local axes from the global ones can be expressed as

$$\alpha_{0ab} = \gamma_{0ab} - \beta_{0ab} \quad (126)$$

where

$$\gamma_{0ab} = \arctan \frac{z_b^G - z_a^G}{x_b^G - x_a^G} \quad (127)$$

is the angle between the beam chord (straight line connecting the end joints) and the global axis x^G , and β_{0ab} is the angle between the beam chord and the tangent to the centerline at the left end; see Fig. 2. Recall that (x_a^G, z_a^G) and (x_b^G, z_b^G) are the global coordinates of the end joints a and b in the initial state.

Strictly speaking, formula (127) gives the correct result only if $x_b^G > x_a^G$ and, to make it general, the rule for evaluation of γ_{ab} would need to be split into several cases. However, for evaluation of the transformation formulae we will not really need the angle γ_{0ab} as such but rather its sine and cosine, which are conveniently expressed as

$$\cos \gamma_{0ab} = \frac{x_b^G - x_a^G}{L_{ab}} \quad (128)$$

$$\sin \gamma_{0ab} = \frac{z_b^G - z_a^G}{L_{ab}} \quad (129)$$

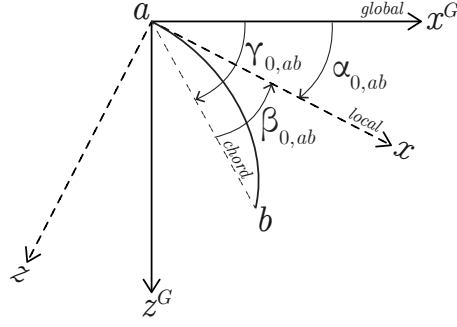


Fig. 2 Local and global coordinate axes in the initial state and definition of angles $\alpha_{0,ab}$, $\beta_{0,ab}$ and $\gamma_{0,ab}$

where

$$L_{ab} = \sqrt{(x_b^G - x_a^G)^2 + (z_b^G - z_a^G)^2} \quad (130)$$

is the initial chord length (distance between the end joints). These equations give the correct values of $\cos \gamma_{0ab}$ and $\sin \gamma_{0ab}$ including the signs for arbitrary inclinations of the chord.

In a similar fashion, the sine and cosine of angle β_{0ab} between the beam chord and the local axis (in the initial state) can be expressed as

$$\cos \beta_{0ab} = \frac{L + u_{s0}(L)}{L_{ab}} \quad (131)$$

$$\sin \beta_{0ab} = \frac{w_{s0}(L)}{L_{ab}} \quad (132)$$

Consistency requires that

$$(L + u_{s0}(L))^2 + w_{s0}^2(L) = L_{ab}^2 \quad (133)$$

Recall that L is the length of the beam measured along the curved centerline while the chord length L_{ab} represents the distance between the end joints, both in the initial stress-free state.

3.5 Matrix formalism and stiffness matrix

It is convenient to rewrite relations (118)–(122) in the matrix notation:

$$\mathbf{u}_b = \mathbf{T}(\varphi_a^G)(\mathbf{u}_b^G - \mathbf{u}_a^G) + \mathbf{l}(\varphi_a^G) \quad (134)$$

$$\mathbf{f}_{ab}^G = \mathbf{T}^T(\varphi_a^G)\mathbf{f}_{ab} \quad (135)$$

where

$$\mathbf{T}(\varphi_a^G) = \begin{pmatrix} \cos(\alpha_{0,ab} - \varphi_a^G) & \sin(\alpha_{0,ab} - \varphi_a^G) & 0 \\ -\sin(\alpha_{0,ab} - \varphi_a^G) & \cos(\alpha_{0,ab} - \varphi_a^G) & 0 \\ 0 & 0 & 1 \end{pmatrix} \quad (136)$$

$$\mathbf{l}(\varphi_a^G) = L_{ab} \begin{pmatrix} \cos(\beta_{0ab} + \varphi_a^G) - \cos \beta_{0ab} \\ \sin(\beta_{0ab} + \varphi_a^G) - \sin \beta_{0ab} \\ 0 \end{pmatrix} \quad (137)$$

Recall that \mathbf{f}_{ab} and \mathbf{u}_b are the column matrices of local components defined in (57)–(58). The column matrices of global components are defined as

$$\mathbf{u}_a^G = \begin{pmatrix} u_a^G \\ w_a^G \\ \varphi_a^G \end{pmatrix}, \quad \mathbf{u}_b^G = \begin{pmatrix} u_b^G \\ w_b^G \\ \varphi_b^G \end{pmatrix}, \quad \mathbf{f}_{ab}^G = \begin{pmatrix} X_{ab}^G \\ Z_{ab}^G \\ M_{ab} \end{pmatrix} \quad (138)$$

For computing purposes, the coefficients in matrices \mathbf{T} and \mathbf{l} can be expanded into

$$\cos(\beta_{0ab} + \varphi_a^G) = \cos \beta_{0ab} \cdot \cos \varphi_a^G - \sin \beta_{0ab} \cdot \sin \varphi_a^G \quad (139)$$

$$\sin(\beta_{0ab} + \varphi_a^G) = \sin \beta_{0ab} \cdot \cos \varphi_a^G + \cos \beta_{0ab} \cdot \sin \varphi_a^G \quad (140)$$

$$\cos(\alpha_{0,ab} - \varphi_a^G) = \cos \alpha_{0,ab} \cdot \cos \varphi_a^G + \sin \alpha_{0,ab} \cdot \sin \varphi_a^G \quad (141)$$

$$\sin(\alpha_{0,ab} - \varphi_a^G) = \sin \alpha_{0,ab} \cdot \cos \varphi_a^G - \cos \alpha_{0,ab} \cdot \sin \varphi_a^G \quad (142)$$

where $\cos \beta_{0ab}$ and $\sin \beta_{0ab}$ are pre-computed constants given by (131)–(132) and

$$\cos \alpha_{0,ab} = \cos \gamma_{0ab} \cdot \cos \beta_{0ab} + \sin \gamma_{0ab} \cdot \sin \beta_{0ab} \quad (143)$$

$$\sin \alpha_{0,ab} = \sin \gamma_{0ab} \cdot \cos \beta_{0ab} - \cos \gamma_{0ab} \cdot \sin \beta_{0ab} \quad (144)$$

are pre-computed constants obtained from the constants given by (128)–(132).

Combining (134)–(135) with the inverse form of (60),

$$\mathbf{f}_{ab} = \mathbf{g}^{-1}(\mathbf{u}_b) \quad (145)$$

we get

$$\mathbf{f}_{ab}^G = \mathbf{T}^T(\varphi_a^G) \mathbf{g}^{-1}(\mathbf{T}(\varphi_a^G)(\mathbf{u}_b^G - \mathbf{u}_a^G) + \mathbf{l}(\varphi_a^G)) \quad (146)$$

This formula summarizes the process of evaluation of the left-end forces and moment from the end displacements and rotations. For better clarity, let us rewrite it in the simplified form

$$\mathbf{f}_{ab}^G = \mathbf{T}^T \mathbf{g}^{-1}(\mathbf{T}(\mathbf{u}_b^G - \mathbf{u}_a^G) + \mathbf{l}) \quad (147)$$

bearing in mind that matrices \mathbf{T} and \mathbf{l} depend on the left-end rotation, φ_a^G , which is at the same time the last component of column matrix \mathbf{u}_a^G .

The dependence of \mathbf{T} and \mathbf{l} on φ_a^G needs to be taken into account when developing the relation between infinitesimal increments of end displacements and end forces, which will provide an appropriate formula for the tangent element stiffness matrix.

The linearized form of equations (134)–(135) reads

$$d\mathbf{u}_b = \mathbf{T}(d\mathbf{u}_b^G - d\mathbf{u}_a^G) + \left(\mathbf{T}'(\mathbf{u}_b^G - \mathbf{u}_a^G) + \mathbf{l}' \right) d\varphi_a^G \quad (148)$$

$$d\mathbf{f}_{ab}^G = \mathbf{T}^T d\mathbf{f}_{ab} + \mathbf{T}'^T \mathbf{f}_{ab} d\varphi_a^G \quad (149)$$

where

$$\mathbf{T}' = \frac{\partial \mathbf{T}(\varphi_a^G)}{\partial \varphi_a^G} = \begin{pmatrix} \sin(\alpha_{0,ab} - \varphi_a^G) - \cos(\alpha_{0,ab} - \varphi_a^G) & 0 \\ \cos(\alpha_{0,ab} - \varphi_a^G) & \sin(\alpha_{0,ab} - \varphi_a^G) & 0 \\ 0 & 0 & 0 \end{pmatrix} \quad (150)$$

$$\mathbf{l}' = \frac{\partial \mathbf{l}(\varphi_a^G)}{\partial \varphi_a^G} = L_{ab} \begin{pmatrix} -\sin(\beta_{0ab} + \varphi_a^G) \\ \cos(\beta_{0ab} + \varphi_a^G) \\ 0 \end{pmatrix} \quad (151)$$

Combining this with the linearized version of (145),

$$d\mathbf{f}_{ab} = \mathbf{G}^{-1}(\mathbf{u}_b) d\mathbf{u}_b \quad (152)$$

we get

$$\begin{aligned} d\mathbf{f}_{ab}(\varphi_a^G) &= \mathbf{T}^T \mathbf{G}^{-1} [\mathbf{T}(d\mathbf{u}_b^G - d\mathbf{u}_a^G) + [\mathbf{T}'(\mathbf{u}_b^G - \mathbf{u}_a^G) + \mathbf{l}'] d\varphi_a] + \mathbf{T}'^T \mathbf{f}_{ab} d\varphi_a = \\ &= \mathbf{T}^T \mathbf{G}^{-1} \mathbf{T}(d\mathbf{u}_b^G - d\mathbf{u}_a^G) + [\mathbf{T}^T \mathbf{G}^{-1} [\mathbf{T}'(\mathbf{u}_b^G - \mathbf{u}_a^G) + \mathbf{l}'] + \mathbf{T}'^T \mathbf{f}_{ab}] d\varphi_a \end{aligned} \quad (153)$$

where \mathbf{G}^{-1} is the inverse of Jacobi matrix \mathbf{G} evaluated at $\mathbf{f}_{ab} = \mathbf{g}^{-1}(\mathbf{u}_b)$ where $\mathbf{u}_b = \mathbf{T}(\mathbf{u}_b^G - \mathbf{u}_a^G) + \mathbf{l}$.

Based on (153), we can set up the first three rows of the 6×6 element tangent stiffness matrix (in global coordinates). In view of (123)–(124), the fourth row is minus the first row, and the fifth row is minus the second row, because $dX_{ba}^G = -dX_{ab}^G$ and $dZ_{ba}^G = -dZ_{ab}^G$. To determine the sixth row, one needs to linearize the expression for M_{ba} . Instead of using (125), it is convenient to set up an equivalent formula written in terms of the global components. From the moment equilibrium condition written with respect to the centroid of the right end section in the deformed state, we get

$$M_{ba} = -M_{ab} + X_{ab}^G(z_b^G - z_a^G + w_b^G - w_a^G) - Z_{ab}^G(x_b^G - x_a^G + u_b^G - u_a^G) \quad (154)$$

and the infinitesimal increment of the right-end moment can be expressed as

$$\begin{aligned} dM_{ba} &= -dM_{ab} + (z_b^G - z_a^G + w_b^G - w_a^G)dX_{ab}^G - (x_b^G - x_a^G + u_b^G - u_a^G)dZ_{ab}^G + \\ &\quad + X_{ab}^G(dw_b^G - dw_a^G) - Z_{ab}^G(du_b^G - du_a^G) \end{aligned} \quad (155)$$

Consequently, the sixth row of the stiffness matrix can be constructed as a linear combination of the first three rows with coefficients $(z_b^G - z_a^G + w_b^G - w_a^G)$, $-(x_b^G - x_a^G + u_b^G - u_a^G)$ and -1 , resp., added to the row $(Z_{ab}^G, -X_{ab}^G, 0, -Z_{ab}^G, X_{ab}^G, 0)$. However, this does not even have to be done, since the stiffness matrix must be symmetric and we already have its sixth column, except for the last (i.e., diagonal) entry. So it is sufficient to mirror the entries from the sixth column into the sixth row and put

$$k_{66} = (z_b^G - z_a^G + w_b^G - w_a^G) k_{16} - (x_b^G - x_a^G + u_b^G - u_a^G) k_{26} - k_{36} \quad (156)$$

on the diagonal.

4 Numerical examples

A nonlinear curved beam element based on the proposed approach has been implemented into OOFEM [14, 15], an object-oriented finite element code. Even though the present formulation is not based on an interpolation of displacements and rotations using fixed shape functions multiplied by unknown nodal values, the element can still be incorporated into a structural model in the same way as conventional beam elements. For given input values of nodal (joint) displacements

and rotations, the corresponding end forces and moments are evaluated and assembled into nodal equilibrium equations. Also, the corresponding 6×6 element tangent stiffness matrix is constructed and assembled (by standard procedures) into the structural tangent stiffness matrix used in global equilibrium iterations. The accuracy and efficiency of the suggested approach will now be demonstrated using five examples.

The first three examples treat arches of a circular shape, for which functions φ_0 , u_{s0} and w_{s0} that characterize the initial geometry in terms of the arc-length coordinate are given by (5)–(7). The fourth example deals with a parabolic arch, and it shows that analogous closed-form expressions are in this case not available; therefore, it is explained how the description of the initial geometry can be handled numerically. Finally, the last example analyzes a logarithmic spiral, for which functions (170)–(172) describing the initial geometry are derived in the appendix.

4.1 Symmetric circular arch, initial stiffness

It is well-known that curved finite elements suffer by excessive stiffness unless the axial displacement interpolation is of a sufficiently high order. When low-order axial displacement approximations are used, membrane locking causes a bending-dominated response. This locking mechanism can be eliminated by using selectively reduced integration of the stiffness terms [24, 25].

The present formulation exploits the equilibrium equations in their strong form and does not work with a priori chosen shape functions for the kinematic approximation, unlike standard displacement-based finite elements. The membrane locking effect is therefore not expected to occur and accuracy can be increased simply by increasing the number of integration segments. This can be verified by analyzing the circular arch in Fig. 3a. The same problem was studied by Stolarski and Belytschko, who constructed a geometrically nonlinear model in the spirit of the shallow-shell approximation of Marguerre [11], first for a curved Euler-Bernoulli beam [24] and then for a curved beam with shear distortion [25].

To facilitate the comparison, let us take the geometrical and constitutive parameters from the original papers. They were specified in British units (inches and psi), which will be omitted here. The cross section is a rectangle of width $b_s = 1.2$ and depth $h_s = 0.125$, the radius of the undeformed centerline is $R_0 = 2.935$, and the elastic modulus is set to $E = 1.05 \times 10^7$ (which is the value for aluminum in psi). Symmetry is exploited, and so the numbers of elements reported below always correspond to one half of the structure. On the other hand, the applied force P is considered as the full load on the whole structure.

The complete load-deflection curve is nonlinear but locking phenomena can be detected already in the geometrically linear range, where the structural response is conveniently characterized by the load-deflection ratio, P/w , playing the role of the initial structural stiffness (i.e., the initial slope of the nonlinear load-deflection diagram). Here, w denotes the vertical deflection under the loading force, P . In [24], the analytical value of the P/w ratio for the Euler-Bernoulli model was reported to be equal to 471.09, but this value was actually based on the load acting on one half of the structure and in [25] it was corrected to 942.2. However, our calculation based on the force method indicates that, for a model that neglects the shear distortion and takes into account the axial and flexural deformation, the

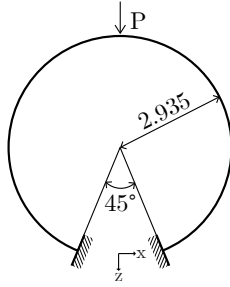


Fig. 3 Symmetric circular arch: geometry

analytically derived stiffness is 943.73. In this calculation and also in the numerical simulations, the interaction between bending and axial deformation is neglected, to be consistent with the model used in the original papers by Belytschko and Stolarski. This means that the “exact” expressions (34)–(35) are replaced by the standard relations $N = EA\varepsilon_s$ and $M = EI\Delta\kappa$, valid for straight beams. If the effect of shear distortion is added, the stiffness decreases to 941.11 for Poisson ratio $\nu = 0.3$ and the effective shear area equal to the actual area, as specified in [25]. With the shear area reduction factor set to the standard value for a rectangle, i.e., $5/6$, the resulting stiffness would be 940.59.

The results presented in [24] showed that a simulation on a mesh composed of eight curved finite elements with a linear approximation of the displacement component in the direction of the chord and a cubic approximation of the displacement perpendicular to the chord leads to an excessive structural stiffness if the integration scheme uses 4 or 3 Gauss integration points. The resulting P/w ratios were 1396.6 and 1405.1, respectively, which corresponds to relative errors of 48 % and 49 %. Reduced integration with 2 integration points per element resulted into $P/w = 900.26$, which is by 4.6 % lower than the exact value.

In [25], the same problem was analyzed using a slightly adjusted model with shear distortion taken into account and with the effective shear area considered as equal to the actual area. In this case, the theoretical stiffness is 941.11. The displacement-based element used a cubic interpolation for transverse displacements, quadratic for sectional rotations and linear for axial displacements. Eight elements with full integration would again lead to an excessive stiffness (1389.8, 48 % above the exact value) while a 2-point integration (which corresponds to reduced integration of the membrane terms and full integration of the shear terms) gives a substantial improvement (946.6, 0.6 % above). Various hybrid and mixed formulations were tested as well but none of them gave a closer approximation of the analytical result.

In our analyses, we used discretizations by one or two curved elements. It is remarkable that, for the one-element mesh, no global degrees of freedom were needed and the problem was solved simply by prescribing the end displacements and rotations and evaluating the corresponding end forces and moments. For the two-element mesh, only three global unknowns had to be introduced. Accuracy was increased by refining the integration segments and the full nonlinear model

NIS	1 element		NIS	2 elements	
	P/w	error [%]		P/w	error [%]
Exact	943.73				
4	632.01	33.031	2	633.33	32.891
8	839.37	11.058	4	839.82	11.010
16	915.23	3.020	8	915.36	3.007
32	936.44	0.773	16	936.47	0.769
64	941.90	0.194	32	941.91	0.193
128	943.27	0.049	64	943.28	0.048
256	943.62	0.012	128	943.62	0.012
$\rightarrow \infty$	943.73	0.000	$\rightarrow \infty$	943.73	0.000

Table 1 Symmetric circular arch: initial load-deflection ratios and the corresponding errors caused by numerical integration.

was used but the initial load-deflection ratio was evaluated from the stiffness matrix computed in the undeformed configuration.

The results in Tab. 4.1 show that as the number of integration segments (NIS) is increased, the load-deflection ratio converges to the exact value, 943.73. Convergence is monotonic (from below) and fully regular. Asymptotically, quadratic convergence is observed, in the sense that the error is inversely proportional to the square of the NIS (i.e., when the NIS is doubled, the error is reduced by a factor close to 4). Solutions obtained on the one-element and two-element meshes are very similar, provided that the total number of integration segments is kept the same. The relative error obtained with one element divided into 16 integration segments (or for two elements, each divided into 8 segments) is about 3 % and it is lower than the error reported in [24] for 8 finite elements with reduced two-point integration, which required 18 global unknowns.

4.2 Unfolding of a circular cantilever beam

In the previous example, the relation between internal forces and deformation variables was used in its standard form, so that the results could be directly compared to those reported in previous papers. For linear elastic beams, it is usually assumed that the bending moment is not affected by the axial strain and the normal force is not affected by the curvature. However, this can be rigorously proven only if the beam is initially straight. For beams with an initial curvature, we have derived modified relations (34)–(35), which contain modified sectional characteristics and cross-coupling terms. Let us now explain the physical origin of these modifications and illustrate the resulting effects on the structural behavior. For this purpose, we will consider a curved cantilever which has the initial form of a full circle, cut at a certain section. One side of the cut is clamped and the other is loaded by an increasing bending moment, which gradually unfolds the beam to a straight configuration and subsequently folds it again to a circular shape with the opposite curvature.

Even though this fictitious test might seem to be the direct analog of the simple example of a straight cantilever folded to a circle by an end moment [9, 21], the case of the initially curved beam is actually more involved. For pure bending

(i.e., zero normal force) and a rectangular cross section of width b_s and depth h_s , equations (52)–(53) reduce to

$$\varepsilon_s = \frac{\kappa_0 M}{EA} = \kappa_0 \frac{M}{Eb_s h_s} \quad (157)$$

$$\Delta\kappa = \left(\frac{1}{EI_{\kappa_0}} + \frac{\kappa_0^2}{EA} \right) M = \frac{12 + h_s^2 \kappa_0^2 + 0.15 h_s^4 \kappa_0^4}{1 + 0.15 h_s^2 \kappa_0^2} \frac{M}{Eb_s h_s^3} \quad (158)$$

in which $\kappa_0 = 1/R_0$ is the initial curvature. Here we have taken into account that, for the rectangular section, the modified moment of inertia I_{κ_0} can be approximated by formula (42) and the standard sectional characteristics are $A = b_s h_s$ and $I = b_s h_s^3/12$.

For an initially straight cantilever of length $L = 2\pi R_0$, the moment needed to fold the cantilever into a full circle would be $M_0 = EI\kappa_0 = EI/R_0$, and the radius of that circle would be R_0 . On the other hand, if the cantilever in its initial stress-free shape has the form of a circle of radius R_0 , application of moment $-M_0$ (the negative sign means that the moment acts clockwise) leads to the change of curvature

$$\Delta\kappa = -\frac{12 + h_s^2 \kappa_0^2 + 0.15 h_s^4 \kappa_0^4}{1 + 0.15 h_s^2 \kappa_0^2} \frac{EI\kappa_0}{Eb_s h_s^3} = -\frac{12 + h_s^2 \kappa_0^2 + 0.15 h_s^4 \kappa_0^4}{12 + 1.8 h_s^2 \kappa_0^2} \kappa_0 \quad (159)$$

and the resulting curvature

$$\kappa = \kappa_0 + \Delta\kappa = \frac{0.8 h_s^2 \kappa_0^2 - 0.15 h_s^4 \kappa_0^4}{12 + 1.8 h_s^2 \kappa_0^2} \kappa_0 \quad (160)$$

is not zero. For instance, for $h_s = 0.4$ and $R_0 = 1$ we obtain $h_s \kappa_0 = h_s/R_0 = 0.4$ and $\kappa = 0.0101$. To get precisely zero curvature, the applied moment needs to be set to $-M_1$ where

$$M_1 = \frac{12 + 1.8 h_s^2 \kappa_0^2}{12 + h_s^2 \kappa_0^2 + 0.15 h_s^4 \kappa_0^4} EI\kappa_0 = \frac{12 + 1.8 h_s^2 \kappa_0^2}{12 + h_s^2 \kappa_0^2 + 0.15 h_s^4 \kappa_0^4} M_0 \quad (161)$$

Under this load, the initially curved cantilever becomes perfectly straight but its length does not remain equal to the initial centerline length $L = 2\pi R_0$ because the axial strain

$$\varepsilon_{s1} = \frac{\kappa_0}{Eb_s h_s} \cdot (-M_1) = -\frac{h_s^2 \kappa_0^2 + 0.15 h_s^4 \kappa_0^4}{12 + h_s^2 \kappa_0^2 + 0.15 h_s^4 \kappa_0^4} \quad (162)$$

is not zero. For our example with $h_s \kappa_0 = 0.4$, we obtain $\varepsilon_{s1} = -0.0135$.

The physical reason why the circular arch unfolded by a uniform moment into a straight beam tends to shrink is that if it did not, the compressive strain in the fibers that were initially on the outer surface and had initial length $2\pi(R_0 + h_s/2)$ would be $-h_s/(2R_0 + h_s)$ while the tensile strain in the fibers that were initially on the inner surface and had initial length $2\pi(R_0 - h_s/2)$ would be $h_s/(2R_0 - h_s)$, i.e., it would be higher in magnitude than the compressive strain. If the material law is linear elastic, the same would hold for the stresses and the resulting normal force would be tensile. To get zero normal force, the centerline length must be reduced.

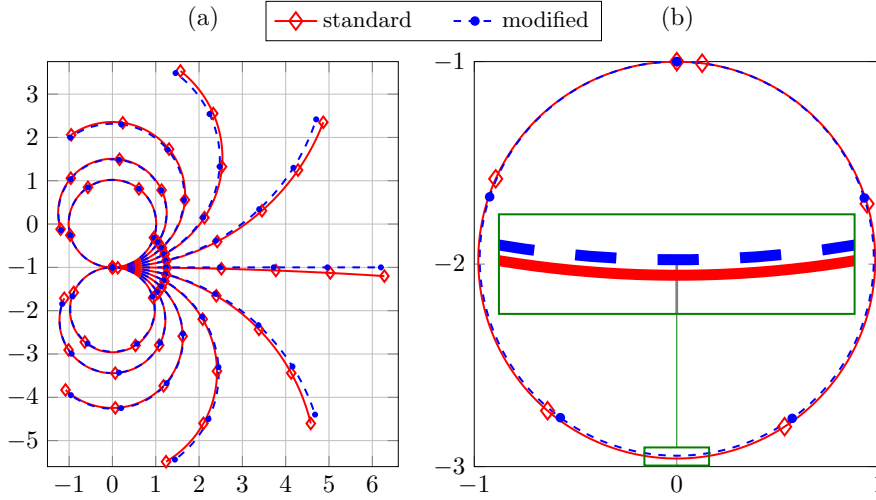


Fig. 4 Comparison of the standard and modified theories for pure bending of a circular cantilever beam: (a) deformed configurations for an increasing end moment ranging from 0 to $-2M_1$, (b) closer look at the final stage.

The case of a fully unfolded circle that still remains linear elastic in terms of the engineering strain and nominal stress may look purely academic, but the same argument applies even to much lower strain levels and thus the centerline would shrink at least during an initial stage of the unfolding process. This phenomenon is neglected by the standard theory, which is in many cases justified because the effect is indeed weak provided that $h_s \kappa_0 \ll 1$. The difference between M_1 and M_0 for $h_s \kappa_0 = 0.4, 0.2, 0.1$ and 0.05 is about 1 %, 0.3 %, 0.07 % and 0.02 %, respectively. However, note that the case of $h_s \kappa_0 = 0.4$ is not outside the range of what is normally considered as slender beams, because the total length of the circular centerline is $L = 2\pi R_0 = 2\pi/\kappa_0$ and thus the span-to-depth ratio of the unfolded cantilever is $L/h_s = 2\pi/(h_s \kappa_0) \approx 15.7$. In fact, the unfolding of a circular cantilever was studied in [8] using the standard theory, with dimensions set to $L = 10$ and $h_s = 1$, which corresponds to $h_s \kappa_0 = 2\pi h_s/L \approx 0.628$. In this case, the described modification would play a significant role and the difference between M_1 and M_0 would be about 2.4 %.

Another (closely related) consequence of the coupling between membrane and bending effects is that if the applied moment is $-2M_1$, the curvature changes from κ_0 to $-\kappa_0$ and one may think that the centerline is located on a circle of radius R_0 (i.e., of the same radius as in the initial state), but in reality the radius is different. The reason is that the curvature corresponds to the derivative of rotation with respect to the arc length coordinate measured along the initial centerline, but the arc length along the deformed centerline is different, since the axial strain is not zero. The actual radius of curvature under loading by constant moment $-2M_1$ leading to curvature $-\kappa_0$ and axial strain $2\varepsilon_{s1}$ is evaluated as

$$R = \left| \frac{(1 + 2\varepsilon_{s1}) dx}{d\varphi} \right| = \frac{1 + 2\varepsilon_{s1}}{\kappa_0} = (1 + 2\varepsilon_{s1}) R_0 \approx 0.973 R_0 \quad (163)$$

This means that if the modified theory is used and moment $-2M_1$ is applied, the resulting shape is a perfectly closed circle of a smaller radius than the initial one, with the radius reduced by approximately 2.7 % (here we consider again our specific example with $h_s \kappa_0 = 0.4$).

The deformed shapes of the initially circular beam that correspond to the applied moment ranging from 0 to $-2M_1$ with step $-0.2M_1$ are shown in Fig. 4. The solid red curves have been obtained using the simple relations $N = EA \varepsilon_s$ and $M = EI \Delta \kappa$ while the dashed purple curves have been obtained with the modified relations (34)–(35). In the middle of the deformation process, at applied moment $M = -M_1$, the current shape computed using the modified theory is straight and the centerline length is slightly reduced as compared to the initial one. On the other hand, according to the standard theory the centerline length would remain constant, and the current shape would be straight at applied moment $M = -M_0$ while at $M = -M_1$ it would be slightly curved. The markers plotted in Fig. 4 indicate the position of points that are initially regularly spaced on the centerline at $s = iL/5$ where $i = 0, 1, \dots, 5$.

The simulations also confirm the theoretical solution that corresponds to the ultimate stage of loading, with applied moment $-2M_1$; see the “lower” circle in Fig. 4a, which is also shown in more detail in Fig. 4b. For the modified theory, the deformed shape plotted by the dashed blue line corresponds to a full circle of radius close to 0.973, as predicted in (163). On the other hand, the standard theory would give a perfectly closed circle of the same radius as the initial one only if moment $-2M_0$ was applied. Under moment $-2M_1$ it gives a deformed centerline located on a circle of radius approximately $0.98 R_0$, plotted in Fig. 4 by the solid red line. As seen in Fig. 4b, this circle is “more than closed”, i.e., the free end of the cantilever initially located at the origin does not end up at the origin but is slightly shifted along the circle clockwise.

To provide not only a visual but also a quantitative assessment, the distances between the positions of the end point computed using the standard and modified theory at different levels of loading are evaluated in Table 2. The distance (i.e., the Cartesian norm of the difference between displacement vectors) is normalized here by the initial radius R_0 , so the values around 0.2 represent a considerable error.

$-M/M_1$	normalized error
0.2	0.0228
0.4	0.0660
0.6	0.1224
0.8	0.1780
1.0	0.2168
1.2	0.2279
1.4	0.2095
1.6	0.1726
1.8	0.1388
2.0	0.1256

Table 2 Pure bending of a circular cantilever beam subjected to an increasing end moment: Evaluation of the error in the displacement of the end point caused by replacement of the modified theory by the standard one (normalized by the circle radius R_0).

The deformed shapes in Fig. 4 and the error values in Table 2 are based on a highly accurate numerical solution with 1 element divided into 2048 integration segments. The dependence of the numerical error on the number of integration segments is illustrated in Table 3. The evaluated quantity w is the vertical displacement of the point initially located at $s = L/2$ caused by the applied moment $-M_1$ or $-2M_1$. At $M = -M_1$, the exact value of this displacement is $w = -2R_0$, where $R_0 = 1$ in our example. At $M = -2M_1$, a highly accurate computation yields $w = -3.94612R_0$. The table confirms that asymptotically the error decreases in inverse proportion to the square of the number of integration segments.

Model	$M = -M_1$		$M = -2M_1$	
	w/R_0	error [%]	w/R_0	error [%]
Exact	-2	-	-3.946122	-
4 segments	-2.221453	11.07265	-4.383040	43.69177
8 segments	-2.052343	2.61715	-4.049401	10.32787
16 segments	-2.012914	0.64570	-3.971593	2.54707
32 segments	-2.003215	0.16075	-3.952468	0.63457
64 segments	-2.000802	0.04010	-3.947707	0.15847
128 segments	-2.000201	0.01005	-3.946518	0.03957
256 segments	-2.000050	0.00249	-3.946221	0.00987
512 segments	-2.000012	0.00060	-3.946147	0.00247
1024 segments	-2.000003	0.00015	-3.946128	0.00057
2048 segments	-2.000001	0.00005	-3.946124	0.00017

Table 3 Pure bending of a circular cantilever beam subjected to end moment $-M_1$ or $-2M_1$: Evaluation of errors in vertical displacement caused by numerical integration along the beam element.

All results presented so far have been obtained for a discretization of the entire circular cantilever by 1 curved element. Consider now the effect of mesh refinement. For curved elements, the initial geometry is reproduced exactly and no extra benefit would be gained by using several elements, provided that the total number of integration segments would remain the same. This has already been illustrated for the previous example in Table 4.1. On the other hand, if the initial circular shape is approximated by straight elements, the initial curvature of each element will be zero and the expressions for internal forces will have the standard form (the information about initial curvature is transformed into jumps in the centerline slope between neighboring elements). Upon mesh refinement, the initial centerline geometry approximated by a polygon will converge to a circle, but the numerical solutions obtained for the deformed shape will converge to a limit that corresponds to the standard theory, which neglects the effect of initial curvature on the relations between internal forces and deformation variables. This paradox is related to the fact that if the curved beam is approximated by straight elements that connect nodes located at the curved centerline, the total length of the polygonal approximation properly converges to the length of the curved centerline, and the length of fibers located at a given nonzero distance from the centerline converges

to the same limit, which is however different from the actual length of those fibers on the curved beam. This fact is schematically illustrated in Fig. 5, which shows the circular arch (Fig. 5a) and its approximation by eight straight elements of the standard type (Fig. 5b). A gradual change of the inclination angle of individual sections is replaced by jumps at element interfaces. The arrangement of rectangular domains representing individual elements leads to gaps and overlaps, the area of which does not vanish in the limit as the element size tends to zero.

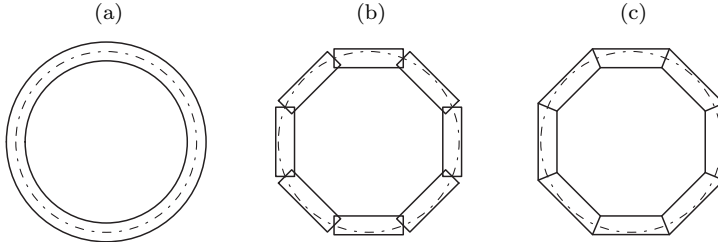


Fig. 5 Geometry of a circular arch: (a) Exact, (b) approximated by straight beam elements with the same length of all longitudinal fibers, (c) approximated by straight beam elements with variable length of longitudinal fibers.

To get the proper limit even with straight elements, one would need to abandon the idea that individual sections are initially perpendicular to the centerline and consider non-parallel end sections as shown in Fig. 5c. In this way, the information on the variable fiber length could be incorporated into the model, but instead of this artificial adjustment it is better to use fully consistent curved elements.

4.3 Asymmetric circular arch, complete load-displacement curve

The third example is representative of an arch instability after large deflections. The structural setup is similar to the arch analyzed in Section 4.1 but the supports are not symmetric and the dimensions are different. This particular structure was investigated by several authors [13, 21, 26] and the solution based on Euler's nonlinear theory of the inextensible curved elastica was evaluated by DaDeppo and Schmidt [5], who reported a value of the maximum load equal to $8.97 EI/R^2$. The theory they used was exact in the sense that no restrictions were imposed on the magnitudes of deflections [4]. The nonlinear boundary-value problem of the inextensible elastica was solved numerically to a high degree of accuracy, which was confirmed by comparisons with certain exact solutions of other problems previously derived by the same authors [3].

The arch is circular with one boundary hinged and the other clamped, and it is loaded by a vertical concentrated load applied at the top, as shown in Fig. 6a. In calculations presented in the literature, the structure was usually considered as very slender, so that the solution obtained for the axially incompressible case with neglected shear distortion could be used as a reference. However, the specific values of parameters are in some cases hard to find.

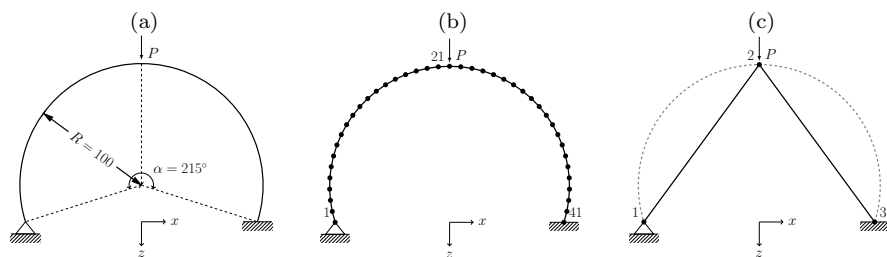


Fig. 6 Asymmetric circular arch: (a) Geometry, (b) forty-element mesh used by Simo and Vu-Quoc [21], (c) two-element mesh used by the present curved beam formulation.

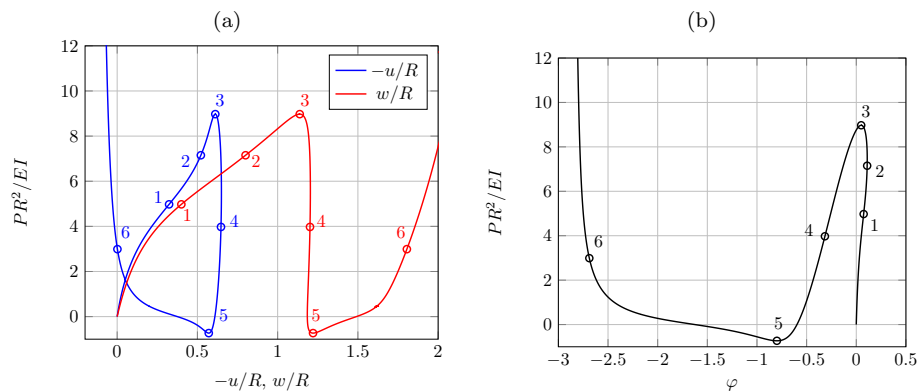


Fig. 7 Asymmetric circular arch: (a) Load-displacement curves and (b) load-rotation curve for the top of the arch (node 2 in Fig. 6c)

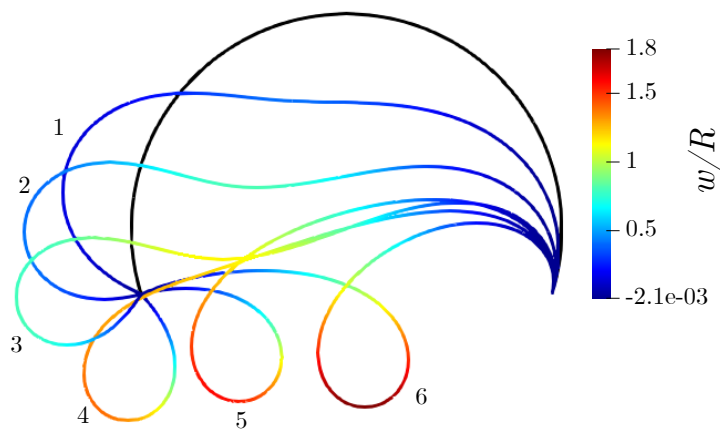


Fig. 8 Asymmetric circular arch: Deformed shapes and normalized vertical displacement along the arch for the six states labeled by numbers 1–6 in Fig. 7.

Wood and Zienkiewicz [26] obtained a buckling load of $9.24 EI/R^2$ using a mesh consisting of sixteen 2D six-noded parilinear elements (linear approximation

in the direction of thickness and quadratic in the longitudinal direction), and one 2D three-noded linear element near the hinged support. Overall, their mesh had 67 nodes with 127 global unknowns, and they analyzed an arch of depth $h_s = 1$, which corresponds to $h_s \kappa_0 = 0.01$.

Simo and Vu-Quoc [21] performed their analysis with a mesh consisting of forty straight beam elements (Fig. 6b) and found a maximum load of $9.0528 EI/R^2$. A similar result was obtained with straight elements by Ibrahimbegović [8], who also reported a great improvement with twenty 3-node curved elements. The resulting maximum load of $8.973 EI/R^2$ was very close to the reference value published by DaDeppo and Schmidt.

In our analysis, we have used the minimum number of elements required to discretize the structure, which results in a two-element mesh shown in Fig. 6c, with only four global unknowns—two displacements and the rotation at the loaded node plus the rotation at the left support. The analysis has been performed under indirect displacement control, with the load iteratively adjusted such that the rotation at the left support increases by prescribed increments. Direct displacement control based on prescribed increments of the vertical displacement under the applied force is not advisable because the corresponding load-displacement diagram, plotted by the red line in Fig. 7a, exhibits a section with a very steep drop and even a slight snapback (see the path 3-4-5 in the figure).

The simulation has been done with the same sectional stiffnesses as in [8], namely $EA = 10^8$ and $EI = 10^6$, which correspond to a section of depth $h_s = \sqrt{0.12} \approx 0.3464$ and thus to $h_s \kappa_0 \approx 0.003464$. The numerical solution naturally depends on the number of segments used for integration of the governing equations on the element level. As seen in Table 4.3, the accuracy of the present simulation is higher than in [26] if 10 integration segments are used and higher than in [21] if 20 integration segments are used.

Further refinement of the integration grid leads again to quadratic convergence. The error is calculated by considering a highly accurate limit value of 8.972922, obtained by refinement until the resulting maximum load stabilizes up to seven valid digits. This limit is in good agreement with the truncated value of 8.97 reported by DaDeppo and Schmidt [5], and it perfectly agrees with the value of 8.973 reported by Ibrahimbegović [8]. One should note that [8] used shear-flexible elements and the actual limit value would be in that case slightly lower.

In the simulations reported in Table 4.3, the standard relations between internal forces and deformation variables have been used. Since, for the given input data, $h_s \kappa_0 \ll 1$, the results obtained with the modified relations would be only slightly different. The maximum load calculated with very high accuracy would change from 8.972922 to 8.972950 if the modified relations are used.

The load-displacement curves plotted in Fig. 7 indicate that the arch exhibits a snap-through behavior after reaching the peak load at the state marked by label 3. The last physically reasonable numerical solution is obtained at the state marked by label 4. The simulation can be continued without problems but the deformed structure passes across the left support (see Fig. 8). This aspect was investigated by Simo et al. [19], who showed that a contact constraint condition on the left support needs to be introduced to obtain a more realistic solution. Here, we have not considered contact activation and the subsequent stiffening effect in the structure because these phenomena are out of scope of the present study.

Model	N° global unknowns	$P_{cr}R^2/EI$	error [%]
DaDeppo and Schmidt [5]		8.97	
Wood and Zienkiewicz [26]	127	9.24	
Simo and Vu-Quoc [21]	117	9.0528	
Ibrahimbegović [8]		8.973	
present approach, 10 segments	4	8.735135	2.650
20 segments	4	8.912875	0.669
40 segments	4	8.957865	0.168
80 segments	4	8.969161	0.0420
160 segments	4	8.971979	0.0105
320 segments	4	8.972686	0.00263
640 segments	4	8.972863	0.00066
$\rightarrow \infty$	4	8.972922	0

Table 4 Asymmetric circular arch: Evaluation of errors in maximum load caused by numerical integration along the beam element and comparison with results from the literature.

4.4 Parabolic arch

In the previous three examples, the initial shape was supposed to be circular and its analytical description was based on formulae (5)–(7). Let us now consider a parabolic arch. In the simplest case, when the left end of the parabolic beam element is located at the apex of the parabola, functions u_{s0} and w_{s0} that characterize the initial undeformed shape must satisfy the equation

$$w_{s0} = \frac{a}{2} (x + u_{s0})^2 \quad (164)$$

where a is a given geometric parameter. These functions are also constrained by the condition

$$(1 + u'_{s0})^2 + w'_{s0}{}^2 = 1 \quad (165)$$

which follows from the fact that differential segments in the fictitious straight configuration have the same length as in the initial undeformed configuration. Taking the derivative of (164) and substituting into (165), we obtain after rearrangement

$$\sqrt{1 + a^2(x + u_{s0})^2} (1 + u'_{s0}) = 1 \quad (166)$$

and integration after separation of variables leads to

$$a(x + u_{s0})\sqrt{1 + a^2(x + u_{s0})^2} + \operatorname{arcsinh}(a(x + u_{s0})) = 2ax \quad (167)$$

This equation implicitly defines function $u_{s0}(x)$ but the closed-form expression for this function is not available. Still, equation (167) could be solved numerically for each prescribed value of x_i and the corresponding $u_{s0}(x_i)$ could be evaluated. In this way, the analytical description of the initial shape would be replaced by a precomputed table of values of x_i and $u_{s0}(x_i)$ for all points of the integration grid. It is then easy to evaluate the corresponding $w_{s0}(x_i)$ from (164) and the “initial rotations $\varphi_0(x_i)$ from

$$\varphi_0(x) = -\arctan a(x + u_{s0}) \quad (168)$$

The procedure described above can be used to ensure uniform spacing of the grid points, which was assumed in the algorithms described in Section 3.3. As an alternative, one can prescribe uniform spacing in projection of the curved beam element onto the local x axis, which coincides with the tangent to the centerline constructed at the left end. In this case, the prescribed values are $x_i + u_{s0}(x_i) = ih_p$, $i = 0, 1, 2, \dots, N$, where $h_p = L_p/N$ is the projected integration segment length derived from the projected element length, L_p . The corresponding values of x_i are then directly obtained from (167) by evaluating the expression on the left-hand side and dividing by $2a$. Afterwards, $u_{s0}(x_i) = ih_p - x_i$ can be determined and the corresponding values $w_{s0}(x_i)$ and $\varphi_0(x_i)$ are calculated as usual from (164) and (168). All this can be done “on the fly” and there is no need to solve nonlinear equations and store a precomputed table of values. In the algorithms, the constant segment length h needs to be replaced by a variable length h_i , computed for each integration segment separately as the Euclidean distance between points with coordinates $((i-1)h_p, w_{s0}(x_{i-1}))$ and $(ih_p, w_{s0}(x_i))$. In theory, this may slightly disturb the quadratic convergence rate when the number of segments increases, since the integration of curvature is no longer based on a central difference scheme. However, no problems have been observed in the specific calculations to be reported next.

For these calculations, we adopt an example of a parabolic arch from [2] and investigate two selected geometries. One, characterized by $H = 0.25$ m, corresponds to a shallow arch, and the other, with $H = 0.5$ m, to a deeper one. The cross section is a square with $b_s = h_s = 0.2$ m and the elastic modulus is $E = 10^4$ MPa.

It is well known that the load-displacement curves of shallow arches typically exhibit snap-through followed by an unstable branch and eventually by restoration of stable equilibrium, while the behavior of deep arches is more complex, with the so-called looping of the load-displacement curve [18]. The aim of this example is to demonstrate that the proposed formulation is able to capture such phenomena. The arch is simply supported and loaded by a concentrated force acting at midspan. Symmetry is exploited and only one half of the arch is simulated, which means that a possible bifurcation into a nonsymmetric shape is ignored.

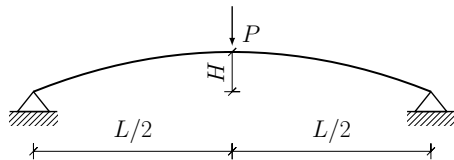


Fig. 9 Parabolic arch: Geometry and loading, with $L = 10$ m, $H = 0.25$ m for the shallow arch and $H = 0.5$ m for the deeper arch.

The response of the shallow arch is described by the diagrams in Fig. 10a,c. The load-displacement curve (Fig. 10a) shows excellent agreement with the results reported in [2], where isogeometric analysis was used. To illustrate the deformation process, the deformed shapes corresponding to four selected states that are marked by special symbols in the load-displacement curve are presented in Fig. 10c: the initial state (black), the state at peak load and onset of snap-through instability

(red), the state at the end of the unstable branch (blue), and a stable state attained at displacement $w = 0.5$ m (green).

In a similar fashion, the response of the deeper arch is described by the diagrams in Fig. 10b,d. In contrast to the shallow arch, the vertical displacement under the load does not increase monotonically and the snapback phenomenon is observed in addition to the snap-through. The simulation cannot be performed under direct displacement control and an arc-length technique is needed. Still, the complicated load-displacement diagram can be captured and the results nicely agree with those from [2].

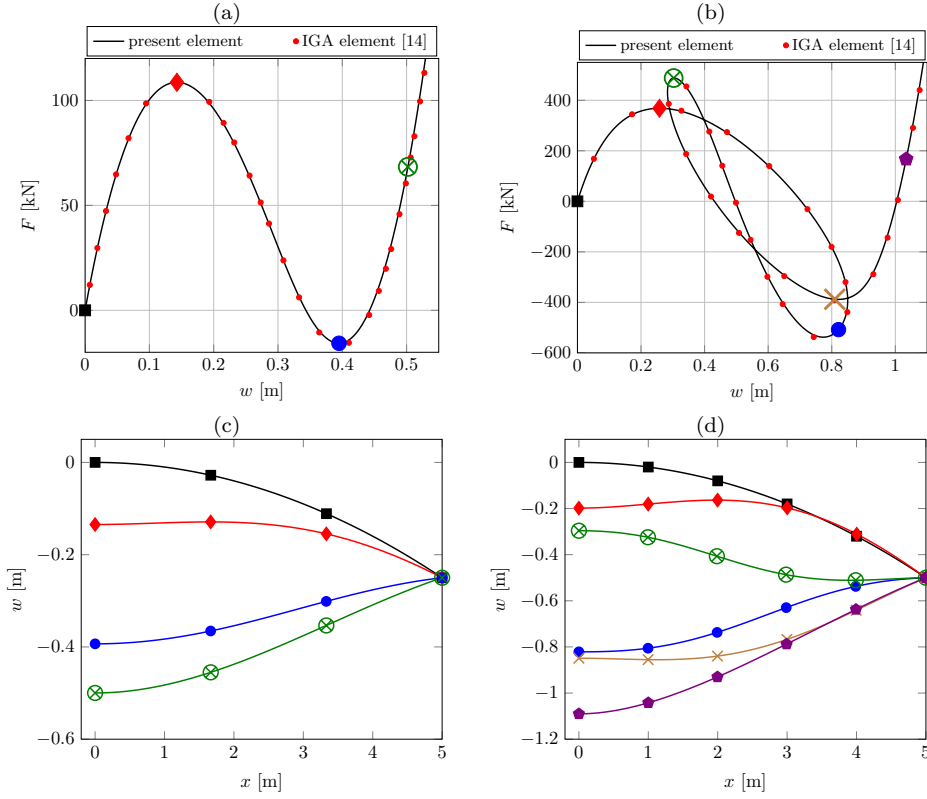


Fig. 10 Parabolic arch: Load-displacement diagrams (a) for the shallow arch and (b) for the deeper arch, and deformed shapes (c) for the shallow arch and (d) for the deeper arch.

4.5 Logarithmic spiral

The last example presents an extreme case of a highly curved beam, which has the initial shape of a planar spiral. It would not be so easy to properly approximate such a “structure” by straight elements or by flat curved elements. Using the present approach, the whole spiral can be represented by one single element and

its shape can be taken into account precisely, independently of the total number of loops.

The spiral considered in this example is a logarithmic one, and in polar coordinates (r, θ) it is described by

$$r = a e^{b\theta} \quad (169)$$

where a and b are positive parameters. Fig. 11 depicts the shape of the spiral obtained for $b = 0.15$ and $\theta \in [0, 4\pi]$. Parameter a sets the length scale and determines the distance of the clamped end of the spiral (at $\theta = 0$) from the pole.

For the logarithmic spiral, it is possible to derive closed-form expressions for functions that describe the initial shape with respect to local Cartesian coordinates with the origin at the left end of the spiral and with the local x axis in the tangential direction. The details of the derivation are provided in the Appendix. The resulting expressions read

$$\varphi_0(x) = \frac{\ln(1 + cx)}{b} \quad (170)$$

$$u_{s0}(x) = a \left((1 + cx) \sin(\varphi_0(x) + \varphi^*) - \sin \varphi^* \right) - x \quad (171)$$

$$w_{s0}(x) = a \left((1 + cx) \cos(\varphi_0(x) + \varphi^*) - \cos \varphi^* \right) \quad (172)$$

where

$$c = \frac{b}{a\sqrt{1 + b^2}} \quad (173)$$

and

$$\varphi^* = \arctan b \quad (174)$$

are auxiliary parameters, introduced only to simplify notation. Formulae (170)–(172) can be understood as a generalized form of the formulae that characterize a circular geometry. Indeed, by setting $a = R$ and $b \rightarrow 0$, we can reduce (170)–(172) to (5)–(7). Since $b \rightarrow 0$ leads to $c \rightarrow 0$, the expression on the right-hand side of (170) tends to a fraction $0/0$ but the limit, x/R , can be properly evaluated using L'Hospital's rule. Formulae (171)–(172) are then reduced simply by setting $a = R$, $c = 0$, $\varphi^* = 0$ and $\varphi_0(x)$ by x/R .

Similarly to Example 4.2, one side of the curved beam is clamped and the other is loaded by an increasing end moment unfolding the spiral, see Fig. 11. Parameter b that controls the shape of the spiral is in this example set to 0.15 and the polar angle θ varies from 0 to 4π , which means that the spiral has initially two full loops. The only other parameter that matters is the ratio $h_s/a = 1/30$, which leads to a dimensionless parameter $EAa^2/EI = 1080$.

Selected deformed shapes (and the initial undeformed shape in black) for a sequence of applied moments ranging from 0 to EI/a are shown in Fig. 12, and the final state, reached at $M = EI/a$, is reproduced in detail in Fig. 13. The spatial coordinates used in Figs. 11–13 have their origin at the pole of the spiral and are normalized by constant a . In the dimensionless coordinates, the clamped section is located at $(-1, 0)$.

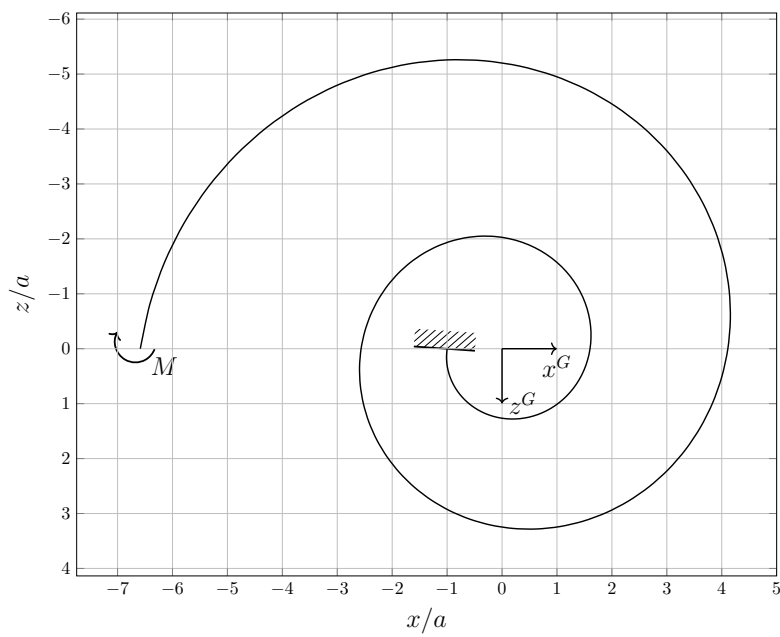


Fig. 11 Logarithmic spiral: Geometric shape, support and loading, and the choice of global coordinate axes

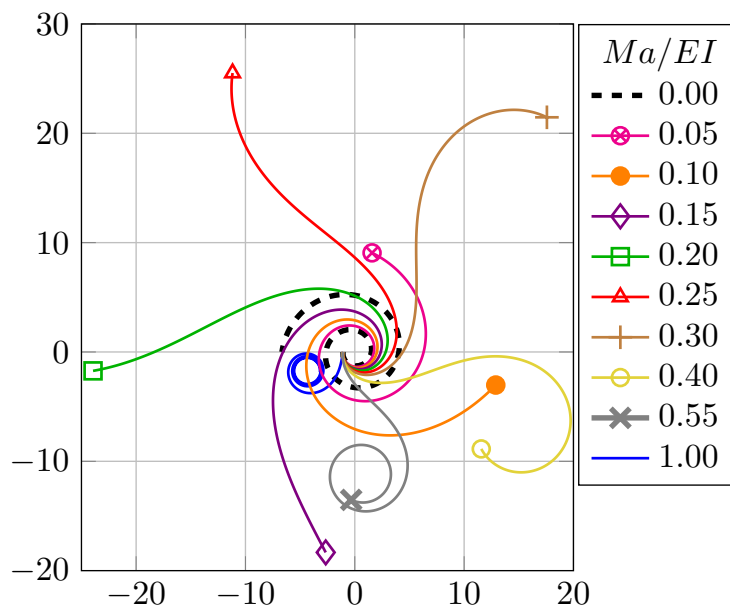


Fig. 12 Initial undeformed shape of the spiral (black) and selected deformed shapes for applied moment increasing up to $M = EI/a$, plotted in the space of dimensionless coordinates normalized by a .

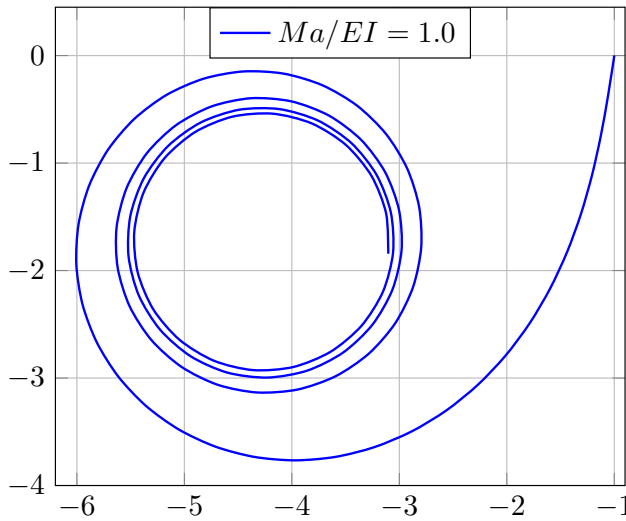


Fig. 13 Deformed shape of the final configuration.

5 Concluding remarks

As illustrated by the examples, the formulation developed in this paper can describe curved elastic beams under large displacements and rotations with high accuracy. In summary, the main idea is that the equilibrium equations are used in their integrated form (45)–(46), and they are combined with the geometrically exact kinematic relations (47)–(49) and sectional equations (50)–(51). The resulting set of three first-order ordinary differential equations is then numerically approximated by an explicit finite difference scheme and the boundary value problem is converted to an initial value problem using the shooting method. On the global (structural) level, the governing equations are assembled in the same way as for a standard two-noded beam element with six degrees of freedom. In this sense, it plays the same role as traditional finite elements in the context of structural analysis. The advantage is that accuracy of the numerical approximation can be conveniently increased by refining the integration scheme on the element level while the number of global degrees of freedom is kept constant.

The specific formulation presented in this paper is based on a number of simplifying assumptions, some of which could be generalized. From the kinematic point of view, the formulation has been developed for curved planar beams assuming the validity of the Navier-Bernoulli hypothesis. An extension to shear-flexible beams would be relatively straightforward. One would need to include the shear force among the internal forces and link it to the sectional shear distortion. This would not substantially affect the structure of the governing equations. A much more challenging task would be an extension to three dimensions, which would require a major change of the descriptor that characterizes the sectional rotation.

The initial shape of the curved beam that can be considered by the present formulation is virtually arbitrary. It is described by functions that relate the position of each centerline point and the inclination of the corresponding section to the

arc-length coordinate. For some shapes, most notably for the circular shape, these functions are available in closed form. If this is not the case, a table of values of these functions can be precomputed numerically. Alternatively, for flat elements, one can use the projection onto a straight line as a replacement of the arc-length coordinate, with the slight drawback that the integration segments along the centerline then do not have a constant length.

Since accuracy can be efficiently improved by increasing the number of integration segments into which the element is divided, the size of the element does not need to be reduced and the number of global degrees of freedom can be kept low and independent of the refinement level. There is of course a limitation stemming from the presently used assumption that the loading is applied exclusively at joints that connect the elements while individual element are not loaded at their intermediate sections. However, this assumption has been introduced only for simplicity and it could easily be removed. In the integrated form of the equilibrium equations, the effect of loads applied directly on the element can be incorporated. This is conceptually easy and the extended implementation only requires a more refined specification and processing of the input data.

From the constitutive point of view, the presented simple version of the method is based on the assumption of linear elasticity. The expressions for internal forces (normal force and bending moment) as functions of the sectional deformation variables (axial stretch or strain and curvature) are then linear and easily invertible. Still, for a curved beam, it is interesting to note that the sectional equations are coupled, in contrast to the case of a straight beam. This phenomenon and its consequences are discussed in detail in the example in Section 4.2. The difference as compared to the standard uncoupled equations is negligible for very slender beams but it may play an important role if, for instance, a thick-walled cylinder is analyzed using a circular beam model.

The constitutive description could be generalized to nonlinear elasticity and even to inelastic behavior (e.g., plasticity). Of course, the computational demands would be increased, because the inverted form of the relation between internal forces and deformation variables would not be described analytically and numerical evaluation, involving an iterative solution of a set of two nonlinear algebraic equations, would need to be adopted. It is fair to admit that the method would fail if this relation becomes non-invertible, e.g., due to softening in the moment-curvature diagram. Such cases would lead to localization phenomena and they would need to be handled by adaptively introducing generalized inelastic hinges.

Acknowledgements The authors are grateful for the support of the Czech Science Foundation (project No. 19-26143X). The authors would also like to thank A. Borković for providing data for the load-displacement curves of parabolic arches calculated by the IGA formulation [2].

Conflict of Interest Statement

The authors declare that the research was conducted in the absence of any commercial or financial relationships that could be construed as a potential conflict of interest.

References

1. Babu C, Prathap G (1986) A linear thick curved beam element. *International Journal for Numerical Methods in Engineering* 23(7):1313–1328, DOI 10.1002/nme.1620230709
2. Borković A, Marussig B, Radenković G (2022) Geometrically exact static isogeometric analysis of arbitrarily curved plane Bernoulli–Euler beam. *Thin-Walled Structures* 170:108,539
3. DaDeppo D, Schmidt R (1969) Nonlinear analysis of buckling and postbuckling behavior of circular arches. *Zeitschrift für angewandte Mathematik und Physik ZAMP* 20(6):847–857
4. DaDeppo D, Schmidt R (1974) Large deflections and stability of hingeless circular arches under interacting loads. *Journal of Applied Mechanics, Transactions ASME* 41(4):989–994
5. DaDeppo D, Schmidt R (1975) Instability of clamped-hinged circular arches subjected to a point load. *Journal of Applied Mechanics, Transactions ASME* 42(4):894–896
6. Ferradi MK, Cespedes X (2021) A curved beam model with the asymptotic expansion method. *Engineering Structures* 241, DOI 10.1016/j.engstruct.2021.112494
7. Ibrahimbegovic A (1997) On the choice of finite rotation parameters. *Computer Methods in Applied Mechanics and Engineering* 149(1):49–71, DOI [https://doi.org/10.1016/S0045-7825\(97\)00059-5](https://doi.org/10.1016/S0045-7825(97)00059-5), containing papers presented at the Symposium on Advances in Computational Mechanics
8. Ibrahimbegović A (1995) On finite element implementation of geometrically nonlinear reissner’s beam theory: three-dimensional curved beam elements. *Computer Methods in Applied Mechanics and Engineering* 122(1):11–26, DOI [https://doi.org/10.1016/0045-7825\(95\)00724-F](https://doi.org/10.1016/0045-7825(95)00724-F), URL <http://www.sciencedirect.com/science/article/pii/004578259500724F>
9. Jirásek M, La Malfa Ribolla E, Horák M (2021) Efficient finite difference formulation of a geometrically nonlinear beam element. *International Journal for Numerical Methods in Engineering* 122(23):7013–7053, DOI <https://doi.org/10.1002/nme.6820>
10. Magisano D, Leonetti L, Madeo A, Garcea G (2020) A large rotation finite element analysis of 3d beams by incremental rotation vector and exact strain measure with all the desirable features. *Computer Methods in Applied Mechanics and Engineering* 361:112,811, DOI <https://doi.org/10.1016/j.cma.2019.112811>
11. Marguerre K (1938) Zur Theorie der gekrümmten Platte grosser Formänderung. In: *Proc. 5th Int. Congress Appl. Mech.*, pp 93–101
12. Marino E, Kiendl J, De Lorenzis L (2019) Isogeometric collocation for implicit dynamics of three-dimensional beams undergoing finite motions. *Computer Methods in Applied Mechanics and Engineering* 356:548–570, DOI <https://doi.org/10.1016/j.cma.2019.07.013>
13. Noor A, Peters J (1981) Mixed models and reduced/selective integration displacement models for nonlinear analysis of curved beams. *International Journal for Numerical Methods in Engineering* 17(4):615–631, DOI 10.1002/nme.1620170409
14. Patzák B (2012) OOFEM—an object-oriented simulation tool for advanced modeling of materials and structures. *Acta Polytechnica* 52(6)

15. Patzák B, Bittnar Z (2001) Design of object oriented finite element code. *Advances in Engineering Software* 32(10-11):759–767
16. Reissner E (1972) On one-dimensional finite-strain beam theory: the plane problem. *Zeitschrift für angewandte Mathematik und Physik ZAMP* 23(5):795–804
17. Reissner E (1973) On one-dimensional large-displacement finite-strain beam theory. *Studies in Applied Mathematics* 52(2):87–95
18. Sabir A, Lock A (1973) Large deflexion, geometrically non-linear finite element analysis of circular arches. *International Journal of Mechanical Sciences* 15(1):37–47
19. Simo J, Wriggers P, Schweizerhof K, Taylor R (1986) Finite deformation post-buckling analysis involving inelasticity and contact constraints. *International journal for numerical methods in engineering* 23(5):779–800
20. Simo JC (1985) A finite strain beam formulation. The three-dimensional dynamic problem. I. *Computer Methods in Applied Mechanics and Engineering* 49(1):55–70
21. Simo JC, Vu-Quoc L (1986) A three-dimensional finite-strain rod model. Part II: Computational aspects. *Computer Methods in Applied Mechanics and Engineering* 58(1):79–116
22. Simo JC, Vu-Quoc L (1986) On the dynamics of flexible beams under large overall motions-the plane case: Part i. *Journal of Applied Mechanics, Transactions ASME* 53(4):849–854, DOI 10.1115/1.3171870
23. Simo JC, Vu-Quoc L (1986) On the dynamics of flexible beams under large overall motions-the plane case: Part ii. *Journal of Applied Mechanics, Transactions ASME* 53(4):855–863, DOI 10.1115/1.3171871
24. Stolarski H, Belytschko T (1982) Membrane locking and reduced integration for curved elements. *Journal of Applied Mechanics, Transactions ASME* 49(1):172–176, DOI 10.1115/1.3161961
25. Stolarski H, Belytschko T (1983) Shear and membrane locking in curved C^0 elements. *Computer Methods in Applied Mechanics and Engineering* 41(3):279–296, DOI 10.1016/0045-7825(83)90010-5
26. Wood RD, Zienkiewicz O (1977) Geometrically nonlinear finite element analysis of beams, frames, arches and axisymmetric shells. *Computers & Structures* 7(6):725–735
27. Zhang C, Di S (2003) New accurate two-noded shear-flexible curved beam elements. *Computational Mechanics* 30(2):81–87, DOI 10.1007/s00466-002-0367-2

A Logarithmic spiral: Description of the initial shape

The logarithmic spiral is easily defined in polar coordinates by equation (169) but the algorithm developed in Section 3 works with local Cartesian coordinates aligned with the curved element. The initial deviation from a straight shape needs to be described by functions that depend on the coordinate measured as the arc length along the undeformed centerline. The purpose of this appendix is to show the derivation of these functions.

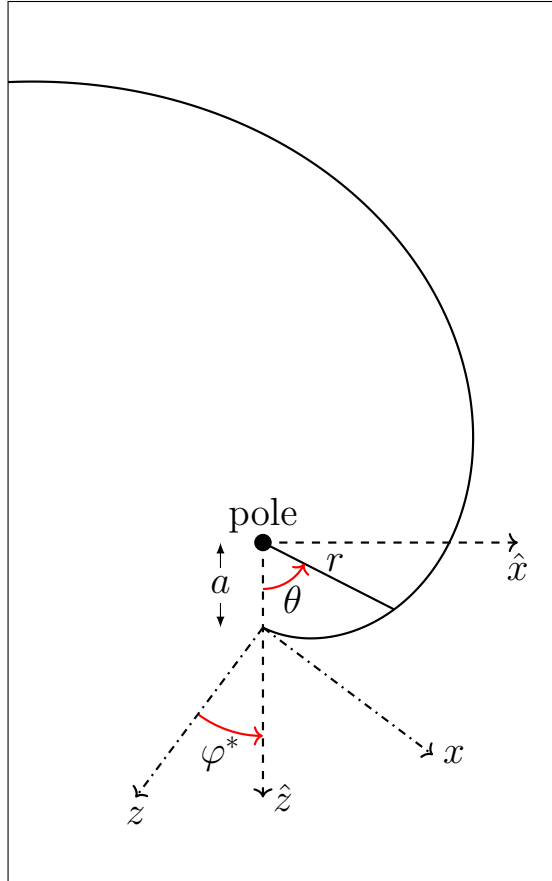


Fig. 14 Geometry of the logarithmic spiral and position of the auxiliary Cartesian axes \hat{x} and \hat{z} and of the local Cartesian axes x and z aligned with the left end of the element (illustrative plot with $b = 0.5$, leading to a faster increase of the radial coordinate than for $b = 0.15$ considered in the example).

In the first step, we can easily express Cartesian coordinates with respect to an auxiliary coordinate system with the origin placed at the pole of the polar coordinates and with axis \hat{z} considered as the axis from which the polar angle is measured counterclockwise; see Fig. 14. Since the radial coordinate is a given exponential function of the polar angle, the Cartesian coordinates can be expressed

as unique functions of the polar angle:

$$\hat{x} = r \sin \theta = ae^{b\theta} \sin \theta \quad (175)$$

$$\hat{z} = r \cos \theta = ae^{b\theta} \cos \theta \quad (176)$$

The final objective is to use the arc-length coordinate s as the independent variable, and so we need to find the link between θ and s . The differential of the arc length is expressed as

$$\begin{aligned} ds &= \sqrt{(d\hat{x})^2 + (d\hat{z})^2} = \\ &= \sqrt{(abe^{b\theta} \sin \theta + ae^{b\theta} \cos \theta)^2 + (abe^{b\theta} \cos \theta - ae^{b\theta} \sin \theta)^2} d\theta = \\ &= a\sqrt{1+b^2} e^{b\theta} d\theta \end{aligned} \quad (177)$$

and integration with initial condition $s = 0$ at $\theta = 0$ leads to

$$s = \frac{a\sqrt{1+b^2}}{b} (e^{b\theta} - 1) = \frac{1}{c} (e^{b\theta} - 1) \quad (178)$$

where $c = b/(a\sqrt{1+b^2})$ is an auxiliary parameter introduced for convenience; see also (173). By inversion of (178) one easily gets

$$\theta(s) = \frac{\ln(1+cs)}{b} \quad (179)$$

and substitution back into (175)–(176) yields

$$\hat{x}(s) = a(1+cs) \sin \theta(s) \quad (180)$$

$$\hat{z}(s) = a(1+cs) \cos \theta(s) \quad (181)$$

It is also useful to express the angle $\hat{\varphi}$ by which the tangent to the spiral deviates (counterclockwise) from the \hat{x} axis, because this at the same time determines the deviation of the cross section from the \hat{z} axis. From

$$\begin{aligned} \cos \hat{\varphi}(s) &= \frac{d\hat{x}(s)}{ds} = ac \sin \theta(s) + a(1+cs) \cos \theta(s) \frac{c}{b(1+cs)} = \\ &= \frac{b}{\sqrt{1+b^2}} \sin \theta(s) + \frac{1}{\sqrt{1+b^2}} \cos \theta(s) \end{aligned} \quad (182)$$

one can infer that

$$\hat{\varphi}(s) = \theta(s) - \varphi^* \quad (183)$$

where $\varphi^* = \arctan b$, as defined in (174). Interestingly, each section deviates from the radial direction by the same angle, φ^* .

The final step consists in transformation of the derived expressions from the auxiliary Cartesian coordinate system aligned with the pole and starting point of the spiral to the local Cartesian coordinate system used by the algorithm, which as its origin at the starting point of the spiral, i.e., at $\hat{x} = 0$ and $\hat{z} = a$, and the x axis is tangent to the spiral at that point. This implies that x and z are rotated clockwise by φ^* with respect to \hat{x} and \hat{z} , and the transformation equations can be written as

$$x = \hat{x} \cos \varphi^* + (\hat{z} - a) \sin \varphi^* \quad (184)$$

$$z = -\hat{x} \sin \varphi^* + (\hat{z} - a) \cos \varphi^* \quad (185)$$

Substitution from (180)–(181) then gives

$$x(s) = a \left((1 + cs) \sin(\theta(s) + \varphi^*) - \sin \varphi^* \right) \quad (186)$$

$$z(s) = a \left((1 + cs) \cos(\theta(s) + \varphi^*) - \cos \varphi^* \right) \quad (187)$$

Having derived the description of the initial spiral shape, we can proceed to the interpretation of the results in the notation used in the main body of this paper. In the present derivation, s denotes the arc-length coordinate and $x(s)$ and $z(s)$ specify the local Cartesian coordinates of the point on the centerline at arc-length distance s from the left end. However, the theoretical considerations in Section 2 as well as the numerical techniques described in Section 3 use x instead of s and interpret this symbol as the x coordinate of the point in the fictitious straight configuration, which would arise if the centerline were unfolded without changing its length (see Section 2.1). The position of each centerline point in the initial curved configuration is then described by the differences u_{s0} and w_{s0} with respect to the straight configuration. This means that on the left-hand sides of (186)–(187) we need to replace $x(s)$ by $x + u_{s0}(x)$ and $z(s)$ by $w_{s0}(x)$, and on the right-hand sides s by x . Furthermore, the initial deviation of a generic section from the direction aligned with the left-end section, denoted in Sections 2–3 as φ_0 , is given by $\hat{\varphi} + \varphi^*$ (because the present xz coordinate system is rotated with respect to the $\hat{x}\hat{z}$ coordinate system by φ^* clockwise), and therefore, in view of (183), φ_0 turns out to be equal to the polar angle θ , which is expressed by (179). This leads to equation (170), and we can also replace the symbol $\theta(s)$ on the right-hand sides of (186)–(187) by $\varphi_0(x)$, which finally yields equations (171)–(172).